Finite-Fault Stochastic Simulation of the 2008 Iwate-Miyagi Nairiku, Japan, Earthquake

Jafar Karashi[1], Meghdad Samaei[2], Masakatsu Miyajima[3]

[1] Department of Earthquake Engineering, Azarbaijan Shahid Madani University, Tabriz, Iran.

[2] Department of Civil Engineering, Allame Rafiei Institute of Higher Education, Qazvin, Iran.

[3] School of Geoscince and Civil Engineering, Kanazawa University, Kanazawa, Japan.

Correspond author: Jafar Karashi (jafarkarashi@yahoo.com).

Key Points:

- Finite-fault stochastic method was used to simulate the recorded acceleration time seires and 5% damped pseudo spectral acceleration.
- Source slip models controlled simulated resuls especially at near-filed stations.
- Simulated results were validated by comparing with a groung motion prediction equation.

Abstract

We applied finite-fault stochastic method to simulate the Mw 6.9, 2008 Iwate-Miyagi earthquake at 44 selected Kik-net sites using EXSIM computer code. To investigate the effects of source characteristics on the simulated results, three models were considered: two models with prescribed slip distribution (Model 1 and Model 3) and a model with random slip distribution (Model 2). S-wave regional attenuation indicates obvious difference between fore-arc and back-arc regions which are formed by volcanic front. Site amplification was determined by corrected surface to borehole spectral ratio and Quarter wavelength methods. High frequency decay parameter (kappa) was estimated to be 0.0473 s. The value of 160 bars for stress drop was calculated by minimizing absolute residual of 5% damped pseudo spectral accelerations (PSA). Comparison of the observed and simulated peak ground accelerations and PSAs were performed to investigate the capability of our finite-fault models. The residual models represent that the simulated results by Model 2 are in good agreement with the observations in $f < 3$ Hz, while the other models can better simulate higher frequency motions. We also focused on the effects of slip patches sitting on the fault plane on near-field stations placed in the directions of slip propagation. For these stations, the simulated results by Model 1 and Model 3 were preferred over those of Model 2. Finite-fault models successfully interpreted the real forced motion to AKTH04 where the recorded peak values were abnormal for non-seismological reasons. Finally, the comparison of intensity measures with the GMPEs showed very good agreement.

1 Introduction

At 23:43 UTC on 13 June 2008 (08:43 on 14 June, Japanese standard time) an earthquake of magnitude M_{JMA} 7.2 (Japanese Meteorological Agency [JMA]) struck an inland volcanic mountain area where epicenter was close to the border of Iwate and Miyagi prefectures. The moment magnitude 6.9, which was estimated by Global Centroid Moment Tensor (GCMT), shows that the event was the largest inland crustal earthquake since Hyogo-ken Nanbu (Kobe) earthquake in 1995. The strongest shaking with JMA seismic intensity scale of 6 upper was measured in the Iwate and Miyagi prefectures, and caused some damages. According to the released reports (Kazama et al., 2012), 23 people were killed or missing and 450 were injured. In addition to the destruction of 2000 houses, several seismical phenomena including landslides and derbies occurred especially at Aratozawa and Komanoyu in mountain areas, respectively. Moment tensor solution reported by NIED using F-net data (Fukuyama et al., 1998) defined a trust-fault type which extended from hypocenter to north-northeast (NNE) and south-southwest (SSW). In such mechanisms, it is expected that the stations on the hanging wall side experience higher motions. Associated with this event, station IWTH25 with $R_{JB}=0$ (closest distance to surface projection of fault plane), recorded the highest peak ground acceleration (PGA) of 4022 cm/s^2 on a three-component vector summation, which of this amount, 3866 cm/s^2 is contributed by the vertical component. The reason for such high amplitude of vertical component is described by Aoi et al. (2008) as “trampoline effect”. Station IWTH26 which is located east of the fault plane, recorded the second large PGAs with 1012 cm/s^2 and 864 cm/s^2 in EW and NS directions, respectively. Such high PGAs and complex slip distribution with maximum value of 6.2 meters (Suzuki et al., 2010), and also high stress drop have distinguished this earthquake from other earthquakes with similar magnitudes.

These characteristics encouraged us to investigate the ability of the stochastic finite-fault method in generating recorded ground motions and calibrating parameters of the event. For this purpose, we used the EXSIM computer code (Motazedian and Atkinson, 2005) which has been updated by Boore (2009a). Since the development of stochastic methods, they have been widely used by various researchers (Ameri et al., 2011; Atkinson and Boore, 2006; Ghasemi et al., 2010; Ghofrani et al., 2013; Ugurhan et al., 2012). Stochastic methods have been applied to simulate previous earthquakes, as well as to investigate future earthquake scenarios and to develop Ground Motion Prediction Equations (GMPEs). The stochastic finite-fault approach can simulate motions with frequencies above 1 Hz very well, but Ghofrani et al., (2013) were able to obtain acceptable results in generating low-frequency motions by combining asperities and background fault plane for the 2011 Tohoku, Japan, earthquak. A pure stochastic method as a simple and efficient tool cannot simulate the characteristics of long-period pulses generated by the rupture directivity effect in the near-field records. On the other hand, in comparison with the deterministic and hybrid methods (Graves et al., 2008; Hartzel, 1978; Irikura, 1983, 1986; Kamae et al., 1998; Pitarka et al., 2000), the finite-fault stochastic method does not require complex parameters such as the small earthquake record as the Green's Function (in the deterministic model) and the crustal velocity model (in the Hybrid method). A combination of stochastic simulation and an analytical model (Mavroeidis and Papageorgiou, 2003) is a tool for elimination of stochastic shortage in producing pulse-like shapes in the observed acceleration and velocity waveforms. The capability of this model has been investigated by several studies (Diao et al., 2018; Motazedian and Moinfar, 2006).

In this study, the simulation of ground motions for the 2008 Iwate-Miyagi earthquake was performed using the pure stochastic finite-fault method based on the dynamic corner frequency approach (Motazadian and Atkinson, 2005). We mainly focused on the effects of high slip patches available on the fault plane on the simulated motions. For this purpose, the path and site parameters were estimated using the recorded strong motions and then the stress drop as a source parameter was calculated by trial and error. The calculated path parameters included geometrical spreading, S-wave anelastic attenuation (quality factor) and path duration, and the site parameters included amplification and high frequency attenuation (kappa). Subsequently, using the obtained parameters, the simulation of ground motions for the selected stations was performed and they were compared with the observed motions. For the validation of the results, values of peak ground acceleration (PGA), velocity (PGV) and 5% damped pseudo spectral acceleration (PSA) were compared with results of ground motion prediction equation (GMPE) of Boore et al. (2014).

2 Method

In the stochastic finite-fault method which was first introduced by Beresnev and Atkinson (1998) as FINSIM, the rupture fault plane is divided into several sub-faults and each sub-fault acts as a point source (Boore, 1983, 2003). Then, all the records obtained using the stochastic point source method for each sub-fault are summed together with their time delay in arrival at the site to obtain the main record for the entire fault plane which is as follows:

$$A(t) = \sum_{i=1}^{nl} \sum_{j=1}^{nw} H_{ij} \times a_{ij}(t - \Delta t_{ij}) \ , \qquad (1)$$

where nl and nw are the number of sub-faults along the length and width of the fault plane, respectively. H_{ij} is the scaling factor used to normalize the spectral level at the high frequency band of all sub-faults. Δt_{ij} is the time delay related to the wave propagated by the sub-fault ij to reach the site and a_{ij} is the corresponding acceleration with sub-fault ij. Another parameter for each sub-fault is the seismic moment, which is defined as follows:

$$M_{0ij} = \frac{M_0 \times S_{ij}}{\sum_{i=1}^{nl}\sum_{j=1}^{nw} S_{ij}} \quad , \qquad (2)$$

where M_0 is the seismic moment of the entire fault and S_{ij} is the slip of the sub-fault ij.

One of the disadvantages of the primary model (FINSIM) was the dependence of the simulated results on the dimensions of the sub-faults and consequently the reduction of the radiated energy of the sub-faults at high frequencies. To address this problem, Motazedian and Atkinson (2005) introduced a dynamic corner frequency model as EXSIM. In this model, the corner frequency is a function of the inverse of the rupture area. Since the rupture area is a function of time and increases chronlogically, the frequency content of each sub-fault is also controlled by the rupture time history. The rupture starts from a sub-fault with a high corner frequency and then the corner frequency tends to lower quantities by increasing rupture area. Therefore, the function of dynamic corner frequency of each sub-fault is defined as:

$$f_{0ij} = 4.9\times10^{6}\beta.(\min(N_R(t), P_{area}))^{-1/3}.(\frac{\Delta\sigma}{M_{0ave}})^{1/3} \quad , \qquad (3)$$

where f_{0ij} is the dynamic corner frequency of the sub-fault ij in Hz, $M_{0ave}=M_0/N$ is the average seismic moment of sub-faults in dyn.cm (N=nl×nw), $N_{R(t)}$ represents the number of ruptured sub-faults, β is the shear-wave velocity near the source in km/s, Δσ is the stress drop in bars and P_{area} is the pulsing area. Seismic moment controls low-frequency content, whereas high-frequency content is controlled by the stress drop of sub-faults. As the rupture propagates toward the end of the fault, the number of ruptured sub-faults increases and at the end of the rupture, the dynamic corner frequency reaches its minimum value, which represents the corner frequency equivalent to the entire fault. Therefore, by propagating the rupture and reducing the corner frequency of sub-faults, the radiated energy of the sub-faults is reduced at high frequencies. However, for identical sub-faults, the spectral level in the high frequency band must be the same. To solve this problem, the scaling factor was introduced: (Motazedian and Atkinson, 2005):

$$H_{ij} = \sqrt{\frac{N\sum(\frac{f}{1+(f/f_0)^2})^2}{\sum(\frac{f}{1+(f/f_{0ij})^2})^2}} \quad , \qquad (4)$$

in which f_0 is the corner frequency of the entire fault palne. By applying the above scale factor to the spectrum, the sum of the radiated energy of the sub-fault ij is equal to the sum of the radiated energy of the first sub-fault. As a result, with propagation of the rupture along the fault plane, the sum of the sub-faults energy is constant and only moves toward lower frequencies.

3 Data and Processing

The Iwate-Miyagi earthquake was recorded at 655 strong motion stations (K-Net and Kik-net), having epicentral distances ranging from 3 to 630 km. To calibrate simulation parameters, we applied 213 three-component acceleration records containing 98 surface and borehole Kik-net stations satisfying the following criteria:

1) After applying the cutoff-distance criterion, we removed records with a fault distance of over 220 km. The aforementioned value for this criterion is chosen because the mean values of PGA in log-distance bins are flattened at distances of more than 220 km, therefore records of these distances should be excluded from the catalog (Ghofrani and Atkinson, 2011);

2) We, following Douglas (2003) criteria, did not consider low-quality accelerograms in the analysis; moreover, we excluded the ones without sufficient pre-event.

3) We only considered stations with available shear-wave velocity profile.

The remaining stations had average shear-wave velocity in the uppermost 30 m (V_{S30}) from 128 to 1398 m/s. The average values were obtained from the proposed function by Borcherdt (1992). Shear-wave velocity profile of K-Net stations were only available for depths lower than 20 m, therefore empirical equation of Boore et al. (2011) was applied to estimate V_{S30}. Figure 1 shows the locations of the stations relative to the earthquake epicenter as well as the volcanic front.

Steps for strong motion data correction including baseline correction and filtering were carried out in time and frequency domains, respectively. We used a 4th order Butterworth acausal filter. The low-cut frequency was chosen based on the method of physical plausibility of integrated time series after filtering (Boore, 2009b). In this method, filtering starts at a low filter corner frequency and the shape of the velocity and displacement waveforms are examined. If they are not reasonable (Akkar and Bommer, 2006; Boore and Bommer, 2005), the process is repeated at a higher filter corner frequency until it reaches a reliable waveform (Boore, 2009b). In the NGA project, this method was also used to process records (Chiu et al., 2008; Darragh et al., 2004). To determine the high-cut frequency, the plotting Fourier acceleration spectrum (FAS) on a log-linear scale can be used. In this case, the Fourier spectrum starts to fall at frequencies above the corner frequency toward higher frequencies until it touches the noise level. The high-cut is the frequency to which this noise level is reached (Anderson and Hough, 1984).

It should be noted that the simulation was performed for 44 stations (blue triangles in Figure1) of the Kik-net network whose characteristics are summarized in Table S1. The selection of these stations was based on shear-wave velocity profiles. In this way, for stations with a low thickness (less than 10 m) soft soil layer near the surface on a homogeneous hard layer with the possibility of strong impedance contrast, simulations were not carried out, because the impact of the surface layer with low shear-wave velocity causes a considerable difference between the observed and simulated ground motions, especially at frequencies below 3 Hz. Therefore, only 44 stations with relatively constant shear-wave velocity variations with increasing depth were considered so that there would be a better calibration of the simulation parameters, especially the stress drop.

Having processed the records, we calculated the geometric mean of the two horizontal components of peak ground acceleration (PGA), peak ground velocity (PGV) and 5% damping pseudo spectral acceleration (PSA). We computed the PSAs at 50 points with a logarithmic distribution from 0.1 to 20 Hz for all records.

4 Input Parameters of Finite-Fault Simulation

In the following, the parameters that were used as input for EXSIM computer code are described. These parameters include source, path, and site which are summarized in Table 1.

4.1 Source Parameters

The input parameters of the source include moment magnitude, stress drop, fault plane geometry, sub-fault dimensions, and location of rupture starting point on the fault plane. In order to estimate the seismic moment and static corner frequency, the displacement source spectra of the borehole records of the Kik-net stations for which the shear-wave velocity exceeds 2000 m/s, were used, where the amplification of the site was close to unity. Only far-field records were used to eliminate the directivity effects. Finally, by removing the propagation-path effects including geometrical spreading and quality factor (equation 8 in section 4.2) from the Fourier displacement spectra, the source spectra was obtained as shown in Figure 2. By matching the Brune's model (Brune, 1970) to the source spectra at low and high frequencies, the seismic moment and the static corner frequency were obtained, respectively. The seismic moment value was 2.75×10^{19} N.m, which is in good agreement with the values introduced by Suzuki et al. (2010) and Asano and Iwata (2011). Using equation presented by Hanks and Kanamori (1979), a moment magnitude of 6.9 was obtained. The static corner frequency was also 0.09 Hz.

We performed the simulations based on three different source models. In Model 1, the results released by Suzuki et al. (2010) were used (Figure 3a) in which the moment magnitude was 6.9 and the rupture starting point was at 39.027°N, 140.878°E and 6.5 km depth. In this model the fault plane with 40×18 km dimensions was divided into 180 square sub-faults with 2 km dimensions. Its strike and dip were also 209° and 40°, respectively. Suzuki et al. (2010) applied kinematic waveform inversion method for near-field strong motions to obtain slip distribution on the fault plane. Slip value on each sub-fault controls its seismic moment. Slip propagation indicated that there are two significant slip patches. The first patch (hereafter patch A1, patch A of Model 1) extendes from the hypocenter to the southern shallower section of the fault plane with a maximum slip of 6.2 m. In addition, the other patch (hereafter patch B1, patch B of Model 1) is observed in the northern part of the fault plane with a maximum slip of 4.4 m which can affect the recorded ground motions at stations located in the northern part of the fault plane. We set shear-wave velocity near the source, crustal density and rupture propagation velocity to 3.6 km/s, 2.8 gr/cm^3 and $0.5\times\beta$, respectively by referring to the rupture inversion model. For Model 2, we used the fault plane geometry presented in the first model and a random slip distribution. This model was used to investigate the validity of random slip distribution for predicting future earthquakes, especially in the near fault zone. The source model introduced by Asano and Iwata (2011) was selected as Model 3 (Figure 3b). The model also had a moment magnitude of 6.9, while the earthquake hypocenter was located at a greater depth (7.8 km) than previous models and at 39.030°N, 140.881°E. In Model 3, a planar fault plane that extended 38 km in strike direction (209°) and 18 km in dip direction (51°) was assumed. The slip distribution on the fault plane shows that there is only one slip patch (hereafter patch A3, patch A of Model 3) with maximum slip of 6 m. The slip propagation on this patch starts from the earthquake hypocenter and continues to the southern surface part of the fault plane. In contrast to Model 1, the rupture propagation velocity has been set to $0.67\times\beta$ in this model. The described patches of Model 1 and Model 3 are illustrated in Figure 3 with dashed blue rectangles.

Another parameter of the source is the percentage pulsing area that indicates how much of the fault plane has slipped at any moment in time. Given that this parameter affects only low frequency motions (less than 1 Hz) to a very small extent (Motazedian and Atkinson, 2005), a 50% value was chosen in this study which is very common. To determine the best value of the stress drop, which controls the energy of motions at high frequencies, the algorithm presented by Ghofrani et al. (2013) was used. Thus, the stress drop that minimizes the absolute residual value was chosen. The residual is defined by:

$$res(f, R_{rup}) = \log_{10}(PSA_{obs}) - \log_{10}(PSA_{sim}) \ , \qquad (5)$$

where f is the frequency of ground motion and R_{rup} is the fault distance. The absolute residual is as follows:

$$\overline{|res|} = \frac{1}{N_f N_d} \sum_{n=1}^{N_f} \sum_{m=1}^{N_d} \left| res(f, R_{rup}) \right| \ , \qquad (6)$$

The standard deviation is also defined as follows:

$$std = \left\{ \frac{1}{N_f} \sum_{1}^{N_f} \mathrm{var}_n \left[res_n(f, R_{rup}) \right] \right\}^2 \ , \qquad (7)$$

where N_f is the number of frequencies, N_d the number of distances, and var_n is the calculated variance of residual vector at the n-th frequency distributed over distance.

4.2 Path Parameters

Earthquake waves decay in the propagation path from the source to the site; this decay is controlled by geometrical spreading and quality factor in stochastic simulation methods. When an earthquake releases energy from its source, waves propagate in all directions. Amplitude of the propagated waves decreases by increasing distance from the source and the area affected by the waves, which is interpreted as geometrical spreading. The most common attenuation modeling that results from the scattering of waves and internal friction of materials (due to nonlinear behavior) is the use of quality factor. In this case, the amount of attenuation is related to the inverse of the quality factor. Boore (2003) described the general functional form of path spectrum as follows:

$$Z(R).\exp\left[-\pi f R / Q(f) \beta\right] , \qquad (8)$$

where Z(R) is the geometric spreading, R is the hypocentral distance, and Q(f) is the quality factor. In this study, the effects of volcanic front in the calculation of path attenuation parameters were considered. The volcanic front is a geological phenomenon that usually occurs along the trench axis and in the subduction zone (Sugimura, 1960). The mantel wedge at the top of the subducted slab is saturated by the upwardly released waters. This area becomes partially melted due to the high mantel wedge temperature, therefore the wave velocity and quality factor are reduced. In this case, the volcanic front divides the region into two parts: fore-arc and back-arc. Propagated waves in the back-arc region are highly attenuated in the mantel wedge (Boore et al., 2009). In Figure 1 the right and left sides of the volcanic front (black dashed line) indicate the fore-arc and back-arc regions, respectively.

The following empirical relationship (Boore et al., 2009) was chosen for regression analysis of ground motion amplitudes (Y, herein FAS) to determine the parameters of geometrical spreading and quality factor using 213 selected surface records:

$$\begin{aligned} &\log_{10} Y = c_1 + c_2 \log_{10}(R) + c_4(R) + c_5 \log_{10}(V_{S30}/V_{ref}) && for \quad R < R_0 \\ &\log_{10} Y = c_1 + c_2 \log_{10}(R_0) + c_3 \log(R/R_0) + c_4(R) + c_5 \log_{10}(V_{S30}/V_{ref}) && for \quad R \geq R_0 \end{aligned} \quad , \qquad (9)$$

$$c_4 = \begin{cases} c_{41} & (1 - ARC) \\ c_{42} & (ARC) \end{cases}$$

where R is the hypocentral distance, R_0 is the fixed crossover distance, V_{S30} represents the mean shear-wave velocity at 30 m uppermost, V_{ref} is the reference shear-wave velocity (= 760 m/s) and c_i (i=1, 2, …, 5) is the regression coefficient. Also, ARC is a dummy variable which equals 1 for fore-arc and 0 for back-arc. The geometrical spreading is usually defined as a multi-segment function. In this study, a two-segment function is used. The coefficients c_2, c_3 and R_0 were used to define the geometrical spreading parameter. To determine the best value for these coefficients, a wide range of values were considered for them; the values which represented the best residual distribution for the Fourier acceleration spectrum, which were -1, -0.5 and 50 km, respectively, were selected. Subsequently, the form of the geometrical spreading is as follows:

$$G(R) = \begin{cases} R^{-1.0} & R < R_0 \\ (50R)^{-0.5} & R \geq R_0 \end{cases} \quad , \qquad (10)$$

the first segment describes direct wave attenuation and the second segment shows the attenuation resulted from wave reflectinos and refractions from Moho discontinuity mixed with a transition to surface-wave spreading (Atkinson and Boore, 2014). The exponential form of $Q = Q_0 f^n$ introduced by Aki and Chouet (1975) was used to determine the S-wave frequency-dependent quality factor parameter (Q) in which Q_0 is the value of the quality factor at frequencies less than 1 Hz and n is the frequency parameter. This parameter was calculated based on the coefficient c_4 obtained from the regression and using the following equation:

$$Q(f) = \frac{-\pi f R}{\ln(10) c_4 \beta} \quad , \qquad (11)$$

in which R is the hypocentral distance and β is the shear-wave velocity along the propagation path assumed to be 3.6 km/s. The quality factor for fore-arc and back-arc was calculated based on the coefficients c_{41} and c_{42}, respectively. The computed Q values for fore-arc and bac-arc regions are illustrated in Figure 4. It is obvious that the quality factor values for fore-arc region in all frequency ranges are lower than values for back-arc region, therefore stations located in the back-arc region have experienced larger attenuation. The values of this parameter are reported in Table 1.

Path duration as one of path parameters influences the simulated waveform amplitude in the time domain. Ground motion duration increases with propagation distance because of crustal seismic wave scattering. In the previous studies (Ghofrani et al., 2013; Motazedian, 2006; Zhang et al., 2016), the method proposed by Atkinson and Boore (1995), $D = D_S + d.R$, had commonly been used. In these models, the total duration (D) had generally been considered to be $D_{5\%-95\%}$ (the time interval corresponding to the Arias intensity reaching 5% and 95% of the total value).

In contrast to previous studies, we applied Boore and Thompson (2014) method, in which total duration is expressed as follows:

$$D = 2.0(D_{5\%-80\%} - D_{5\%-20\%}) \ , \qquad (12)$$

They had two reasons for introducing this model: i) strong P waves cause Arias intensity to reach 5% of total value before shear waves arrival ii) time proportional to Arias intensity reaching 95% of total value increases due to the late arrival of surface waves or existing strong aftershocks. These reasons cause an increase in the computed duration and thus reduce the amplitude of the simulated motions. To calculate the path duration (D_P), it is necessary to subtract the source duration (D_S) from the total duration (D). The source duration is usually assumed to be the inverse of the corner frequency (Atkinson and Silva, 2000). In this study, considering the corner frequency offered in section 4.1, D_S was obtained 11 seconds. The observed path durations for surface records are plotted as a function of hypocentral distance in Figure 5. As can be seen from the data behavior, we decided to use a three-segment model with hinge points at hypocentral distances of 70 and 140 km. The results of the duration model are summarized in Table 1. However, the effects of the volcanic front on the duration model were not investigated in this study since Ghofrani and Atkinson (2015) believed it was negligible.

4.3 Site Parameters

In stochastic simulation methods, the response of the site is modeled by combining the two parameters of amplification and attenuation (Boore, 2003):

$$G(f) = A(f).\exp(-\pi\kappa_0 f) \ , \qquad (13)$$

where A(f) is the amplification of the site and κ_0 is the attenuation factor. Amplification is caused by the propagation of seismic waves from deep layers of soil with high shear-wave velocity and impedance to shallow layers with low shear-wave velocity. In this study, Surface to borehole spectral ratio (SBR) was used to model the amplification of the site. We performed the following procedure to define SBR:

1) Shear wave window (S-wave) of acceleration time series for each record was separated. The window starts with the first arrival of the S-wave and ends when 95% of the total energy reached;

2) A 5% cosine taper function was applied to the S-wave window;

3) FAS of the horizontal components for both surface and borehole recorded accelerations were calculated;

4) Calculated FAS was smoothed using Konno-Ohmachi model (Konno and Ohmachi, 1998);

5) The geometric mean of the smoothed FAS was computed;

6) The surface to borehole spectral ratio (SBR) of each station was calculated;

Destructive interference between upward (incident) and downward (reflected from surface) waves creates a hole in the FAS of borehole records at a particular frequency (Steidl et al., 1996) that creates a spurious resonant peak in the SBR that must be corrected. One of the methods to solve this problem is the use of cross spectrum technique (Safak, 1991; Steidl, 1993). By

multiplying SBR in coherence between surface and borehole records, the corrected surface to borehole spectral ratio (SBRc) is obtained:

$$(SBRc) = \frac{\left|S_{12}(f)\right|^2}{S_{11}(f)S_{22}(f)'}(SBR) \ , \qquad (14)$$

where $S_{11}(f)$ and $S_{22}(f)$ are the power spectral densities of the seismograms recorded at surface and borehole, respectively, and $S_{12}(f)$ is the cross power spectral density function. Empirical method introduced by Cadet et al. (2012) can also be used to remove depth effects. Results of the corrected site amplification are shown in Figure S1. In addition, the site amplification of four stations was obtained from the quarter wave length (QWL) method (Boore, 2003). At three stations AKTH18, IWTH20 and IWTH24, the shear-wave velocity at the borehole accelerometer installation site is low at about 450 m/s (Figure 6b), so using the SBR method can underestimate site amplification and cause a trend in the simulation results. Also the recorded accelerations at surface seismograph of AKTH04 for non-seismological reasons (discussed later) are much higher than not only the adjacent stations but also the nearest station to the fault plane (IWTH25), thus using the SBR method is expected to offer amplification results that are far from reality. Figure 6 depicts the site response obtained from the QWL for the four stations mentioned along with the shear-wave velocity profiles.

Surface layers of soil strongly attenuate the spectral amplitudes at high frequencies, which is interpreted in the form of κ_0. Anderson and Hough (1984) showed that when amplitude spectrum plot is in semi-log scales (amplitude in logarithmic and frequency in linear scales), the spectral amplitude begins to decay linearly at a specific frequency above the corner frequency toward higher frequencies. They suggested the following functional form for this decay:

$$A_0 \exp(-\pi\kappa f) \qquad f > f_E \ , \qquad (15)$$

where A_0 is a constant coefficient, κ is the spectral decay factor, and f_E is the frequency at which the spectrum begins to decrease. They also defined a linear function between kappa and distance as follows:

$$\kappa(R) = \kappa_0 + mR \ , \qquad (16)$$

in which m is the slope, κ_0 is the zero-distance kappa and R is the hypocentral distance. At each station, we calculated the geometric mean κ for the two horizontal components of the surface records and plotted them as a function of the hypocentral distance in Figure 7. The value of the zero-distance intercept is κ_0 that equals to 0.0473 sec. The obtained κ_0 in this study is consistent with the results of Van Houtte et al. (2011) for surface strong motions in Japan.

5 Simulation Results

Using the parameters specified in the previous sections, we performed simulations for the 44 selected stations. In order to eliminate bias due to stochastic variability of the method, simulations were performed in 10 trials for each station. As noted in the source parameters section, the best stress drop value is chosen based on the minimum absolute residuals (equation 6). The residual results showed that the optimized value of 160 bars for stress drop was the most

reliable estimate for the Iwate-Miyagi earthquake. The absolute residuals and standard deviation values for all three models are presented in Table 2. This stress drop is very high compared to similar earthquakes such as 2016 Kumamoto, M_W 7.1, with 64 bars (Zhang et al., 2016), 2016 Meinong, M_W 6.6, with 80 bars (Diao et al., 2018) and 1980 Irpinia, M_W 6.9, with 80 bars (Ameri et al., 2012). This high value of stress drop indicates that strong ground motions of the Iwate-Miyagi earthquake are rich with high frequencies, consistent with observations where large accelerations are recorded at stations near the causative fault.

Figures 8 and 9 show the observed and simulated acceleration waveforms and 5% damped pseudo spectral accelerations at six stations, respectively. The selected stations include three stations with the least distance from the fault plane (IWTH25, IWTH26, IWTH24) as well as three other stations (AKTH19, NIGH02, FKSH14) to cover medium and long distances. IWTH25 with a fault distance of 5 km recorded largest PGAs with 1429 cm/s^2 and 1020 cm/s^2 in EW and NS components, respectively. Model 1 and Model 3 are well able to simulate the peak ground accelerations, whereas the simulated peak value by Model 2 is obviously lower than the observed PGAs. In the frequency domain, three simulation models underestimated PSAs at frequencies above 3 Hz, which is greater for Model 2. IWTH26 which experienced the second largest PGAs with 1012 cm/s^2 and 864 cm/s^2 in EW and NS directions, respectively, is 5.5 km from the fault plane. The same as the results for IWTH25, simulated PGA at IWTH26 by Model 2 is lower than the observed peak values, but the results by Model 1 and Model 3 match well with the observed PGAs. Observed PSAs at IWTH26 are slightly higher than the observed ones by Model 2 at frequencies over than 4 Hz. IWTH24 having a fault distance of 6 km recorded a PGA of 425 cm/s^2 in EW direction and 542 cm/s^2 in NS direction. The PGA introduced by Model 3 is lower than the observed and also simulated PGAs by other models, and cannot reflect the behavior of the recorded motions. The pseudo spectral acceleration observed at IWTH24 is higher at almost all frequencies than predicted by Model 3. At far-filed stations, three simulation models produced an excellent match for the observed and simulated acceleration waveforms and PSAs over all frequency ranges. A comparison of the observed and simulated acceleration time series and 5% damped pseudo spectral accelerations for remaining stations are shown in Figure S2 and S3, respectively.

Overall, it can be summarized that Model 1 can simulate ground motions at all stations well, while Model 2 at IWTH25 and IWTH26 and Model 3 at IWTH24 underestimate the peak ground acceleration and pseudo spectral acceleration especially at high frequencies. Given that the mentioned discrepancies are mostly observed for near-field stations and are somewhat minor for far-field stations, it can be concluded that this difference is due to the slip distribution on the fault plane. To investigate this matter, the location of these three stations along with the projection of slip distribution used in Model 1 and Model 3 are shown in Figure 10. IWTH25 and IWTH26 are located directly above and to the right side of patch A1/patch A3, respectively, where the slip extends from the hypocenter to the southern shallow part of the fault plane. Hence the frequency content of these stations is expected to be strongly affected by this patch. Therefore, the bias in Model 2 may be due to the fact that the random slip model was not capable of producing such a slip patch in that part of the fault plane and thus did not properly simulate the motions at these stations. To match the PSAs simulated and observed by Model 2 at IWTH25 and IWTH26, a stress drop of about 350 bars has to be considered which creates a large trend in the simulated results of the far-field stations. Station IWTH24, located in the northern side of the fault plane, also has conditions similar to the previous stations. Given that the simulated results obtained by Model 1 at IWTH24 are sufficiently consistent with the observed ground motions, it

can be stated that its frequency content is controlled by the slip patch B1 (Figure 10a). As shown in Figure 10b, a high slip area such as patch B1 is not observed in the slip history presented by Model 3 so that its effect would lead to a more accurate prediction of the waveforms and PSAs at IWTH24. The good correlation between the observed and simulated PSAs by Model 2 at station IWTH24 indicates that the random slip model has been able to reliably describe the slip distribution at the location of patch B1.

In the previous section, it was noted that the PGAs recorded at station AKTH04 for non-seismological reasons were very high as its values for EW and NS components were 2199 cm/s^2 and 1318 cm/s^2, respectively. AKTH04 is located in the northwestern of the epicenter, with a fault distance of 18 km (Figure 10). It is obvious that this station is not in the direction of the extending rupture (slip patches), therefore slip propagation cannot be accepted as one of the reasons for the high recorded PGAs. We compared the horizontal accelerations recorded at AKTH04 with the nearest station to the fault plane (IWTH25) to demonstrate the independence of such a high amplitude on the source characteristics. At the borehole, the recorded peak ground accelerations at AKTH04 (265 cm/s2 for EW and 170 cm/s2 for NS) are smaller than those at IWTH25 (655 cm/s2 for EW and 720 cm/s2 for NS). This difference is mainly related to the shorter fault distance of IWTH25. On the other hand, the recorded peak values at ground surface at AKTH04 are much larger than that at IWTH25. Since IWTH25 is closer to the fault plane and the observed motions are also affected by patch A1, the large peak values at AKTH04 can be due to an amplification mechanism in the path of propagation of waves from borehole to ground surface. In order to investigate the effect of surface soil layers on the recorded PGAs at AKTH04, a K-Net station, i.e. AKT023, was also selected for comparison. Figure 10 depicts the position of this station relative to AKTH04. The selected station at a fault distance of 17 km is very close to AKTH04, and the Vs30 difference for these stations reaches about 100 m/s. The mean of recorded peak ground accelerations at surface for AKTH04 is 4.7 times that of AKT023 which is considerable. Given that the distance between the two stations is approximately the same, the low difference in shear-wave velocity cannot account for the high discrepancy in the recorded PGAs for these stations. It is therefore necessary to search for the reasons in non-seismological aspects. By comparing Fourier spectra and maximum amplitude spectra for surface and borehole records, Kamagata and Takewaki (2017) found that high accelerations at this station may be due to irregular interaction between the base-mat and surrounding soil, created at the accelerograph's installation location, whose Investigation does not fall within the scope of this study.

We attempted to generate reliable ground motions at AKTH04 using stochastic simulation. Since the recorded accelerations at the surface are abnormal, the use of SBR method to estimate site amplification is unreasonable, therefore the use of the QWL method based on the existing shear-wave velocity profile was considered (Figure 6). The acceleration time series and the simulated PSAs for all models are plotted in Figure 11 and are compared with the observed values. As it can be seen, the mean of simulated PGAs for the three models is about 345 cm/s^2 which is well below the recorded PGAs at AKTH04. In the frequency domain, PSAs at frequencies above 1 Hz was estimated to be significantly lower. The simulated accelerations for this station are very close to the PGAs recorded at AKT023, which is 360 cm/s^2 for EW and 362 cm/s^2 for NS. Also, there is a very good match between the simulated PSAs at AKTH04 and the observed PSAs at AKT023 (gray curve in Figure 11b) at all frequencies. Based on the comparisons made, the simulated results are expected to largely reflect the actual motions applied to AKTH04.

We provided the residual models between the observed and the simulated 5% damped pseudo spectral acceleration using equation 5 in order to investigate the accuracy of the three simulation models. Figure 12 indicates the average of residuals, and the standard deviation lower and upper bounds. The residual negative values represent an overestimation by the simulation models, whereas the positive values show an underestimation. The behavior of the residual mean for all three models is largely similar. The residual models show that the simulation results for all models at frequencies below 2 Hz overestimate the PSAs but at higher frequencies the opposite is observed. By comparing the models, it is observed that the residual of Model 2 at frequencies below 3 Hz is closer to the zero line, indicating that the simulation accuracy of this model is higher in this frequency range. However, the simulation results obtained from Model 1 and Model 3 at frequencies above 3 Hz are in better agreement with the observed PSAs. Generally, all three models have good capability for simulating far-field motions, but Model 1 takes precedence over simulating near-field motions, especially for stations IWTH24, IWTH25 and IWTH26.

6 Comparison of Observed and Simulated Ground Motions with GMPEs

After simulating the ground motions at the 44 selected stations, we compared the simulated and observed PGAs, PGVs and 5% damped pseudo spectral accelerations at frequencies of 0.5, 1, 5.5 and 10 Hz with the GMPEs proposed by Boore et al. (2014). They developed the GMPEs for calculating medians and standard deviations of average horizontal component intensity measures (PGAs, PGVs and PSAs) for shallow crustal earthquakes in active tectonic regions. The selected empirical equation has been obtained from a global strong motion dataset (NGA-West2 project) with MW 3.0-7.9. For the observed PGAs, PGVs and PSAs, we used the geometric mean for a combination of two horizontal components. Boore et al. (2014) applied Joyner-Boore definition (R_{JB}) to represent the dependence of the intensity measures to distance, therefore we computed R_{JB} for the stations and based on which the comparsions were performed. Figure 13 indicates the medians of GMPEs as a function of R_{JB}, for a reverse faulting style and V_{S30}= 370 m/s that were compared with the observed and simulated intensity measures. The considered shear-wave velocity is the average of V_{S30} for the 44 selected stations. The observed and simulated PGAs, PGVs and PSAs at all frequencies are enclosed in the lower and upper bounds of standard deviation of GMPEs. As shown in Figure 13, the PGAs and PSAs observed at high frequencies at AKTH04 fell outside the lower and upper bounds of had been predicted by the empirical equation, while being in good agreement with the predicted PSAs at lower frequencies. The simulated PSAs for the three models were overestimated at frequencies of 0.5 to 1 Hz compared to the observed values as well as the median of GMPEs. This is consistent with the nature of stochastic simulation techniques that are not well able to generate motions at frequencies below 1 Hz. Another point to mention is that the observed and simulated PGAs and PSAs at higher frequencies show a faster decay than PGVs and PSAs at lower frequencies as the distance increases that is consistent with the GMPEs.

6 Discussion and Conclusion

The 2008 Iwate-Miyagi Nairiku earthquake was the second major inland crustal earthquake in Japan since the Kobe earthquake in 1995, resulting in the highest acceleration

recorded in the strong motion networks, which is 3866 cm/s^2 at the UD component of IWTH25. The Iwate-Miyagi earthquake caused severe damage to buildings and also caused geological phenomena such as liquefaction and landslides in a number of regions. In this study, we used stochastic finite-fault method with dynamic corner frequency approach (EXSIM, Motazedian and Atkinson, 2005) to simulate the recorded ground motions. We also tried to investigate the effect of slip propagation on the simulated motions at near-field stations by applying different source models.

The simulation results are controlled by three parameters of source, path and site. Modeling this event was done by three source models with different slip distributions. For Model 1, the source model presented by Suzuki et al. (2010) was chosen and for Model 2 the previous model but with a random slip distribution was used. The source model introduced by Asano and Iwata (2011) was also selected as Model 3. In the first and third models there are slip patches that strongly affect high frequency motions, especially in near-field stations. We investigated the effects of path parameters using 213 surface recordings. Geometrical spreading, as one of the path parameters, was defined as a two-segment function for distances of less and higher than 50 km. Regional S-wave anelastic attenuation (quality factor) was calculated with respect to the existence of a volcanic front where it divides the study region into two parts: fore-arc and back-arc. For the back-arc region, the quality factor at all frequencies is lower than the fore-arc region, indicating a greater attenuation due to the decrease in shear-wave velocity in the mantel wedge, as the attenuation is inversely proportional to the quality factor. The path duration presented in this study, unlike other previous studies, follows the newer model introduced by Boore and Thompson (2014). To this end, we used a three-segment model with hinge points at 70 and 140 km, given the observed data behavior. The site response is interpreted as one of the input parameters of stochastic simulation methods to a combination of amplification and attenuation caused by the upper layers of soil. The surface to borehole spectral ratio (SBR) and Quarter wavelength (QWL) methods were used to evaluate the site amplification. The SBR method gives an incorrect estimation of amplification due to the presence of a notch in the borehole Fourier spectra caused by the reflected waves from the surface in some records. To fix this error, we applied the cross spectrum technique. The QWL method also provided acceptable results for a number of stations with low shear-wave velocity in the borehole. Zero-distance kappa (κ_0) as the attenuation parameter of site with a value of 0.0473 sec was well able to describe the linear decay trend of PSAs at high frequencies.

In conclusion, the finite-fault stochastic simulation method using the parameters considered has been able to simulate acceleration time series and 5% damped pseudo spectral accelerations for the three models. For the simulated and observed ground motions, a stress drop equal to 160 bars was required to minimize the absolute residual of PSAs. All three models simulated far-field motions well, while for near-field stations the use of prescribed slip models (Model 1 and Model 3) yielded far better results than the random slip model (Model 2). The observed ground motions at IWTH25 and IWTH26, which are located in the direction of slip propagation in patch A1/patch A3, were underestimated by Model 2. The reason may be that the random slip model cannot describe the slip distribution in that section of fault plane. The simulated results for IWTH24 by Model 1 showed that the motions recorded at this station were strongly influenced by the patch B2 at northeast of the fault plane, so the absence of such area in Model 3 has caused an underestimation in the simulated motions. These results show the importance of the slip model on the simulated ground motions especially at near-field stations. In this study, we were able to simulate the actual ground motions applied to AKTH04, where due to

non-seismological reasons the recorded acceleration was very high. The simulated PGA was 345 cm/s^2 (the mean of all three models) which was very close to the PGAs observed at its adjacent station, namely, AKT023. Also the simulated PSAs for the AKTH04 was in very good agreement with the PSAs observed in AKT023. Comparing the three residual models showed that Model 2 at frequencies below 3 Hz, and Model 1 and Model 3 at higher frequencies produced more reliable results. For validation, we compared the simulated and observed results with a GMPEs, which showed excellent agreement for all intensity measures.

Acknowledgments

This work was funded by the JSPS KAKENHI grant JP18KK0129. The authors would like to thank Wataru Suzuki for providing slip data used in Model 1 and Hadi Ghofrani for his help with correction of surface to borehole spectral ratio. The strong ground motion data and site information were obtained from the strong-motion seismograph network at http://www.kyoshin.bosai.go.jp/ (last accessed November 2018). The slip distribution used in Model 3 was downloaded from http://equake-rc.info/srcmod/ (last accessed January 2019). Figures 1, 3 and 10 were plotted by Generic Mapping Tools (Wessel et al. 1991). To prepare other figures, we used graphics software package CoPlot (http://www.cohort.com/, last accessed August 2019).

References

Aki, K., & Chouet, B. (1975). Origin of coda waves: source, attenuation, and scattering effects. *Journal of Geophysical Research, 80(23),* 3322–3342. https://doi.org/10.1029/JB080i023p03322

Akkar, S., & Bommer, J.J. (2006). Influence of long-period filter cut-off on elastic spectral displacements. *Earthquake Engineering and Structural Dynamics, 35(9),* 1145–1165. https://doi.org/10.1002/eqe.577

Ameri, G., Emolo, A., Pacor, F., & Gallovic, F. (2011). Ground-motion simulations for the 1980 M 6.9 Irpinia earthquake (Southern Italy) and scenario events. *Bulletin of the Seismological Society of America, 101(3),* 1136–1151. https://doi.org/10.1785/0120100231

Anderson, J. G., & Hough, S. E. (1984). A model for the shape of the Fourier amplitude spectrum of acceleration at high frequencies. *Bulletin of the Seismological Society of America, 74(5),* 1969–1993.

Aoi, S., Kunugi, T., & Fujiwara, H. (2008). Trampoline effect in extreme ground motion. *Science, 322,* 727–730. https://doi.org/10.1126/science.1163113

Asano, K., & Iwata, T. (2011). Characterization of stress drops on asperities estimated from the heterogeneous kinematic slip model for strong motion prediction for inland crustal earthquakes in Japan. *Pure and Applied Geophysics, 168,*105-116. https://doi.org/10.1007/s00024-010-0116-y

Atkinson, G. M., & Boore, D. M. (1995). Ground motion relations for eastern North America. *Bulletin of the Seismological Society of America, 85(1),* 17–30.

Atkinson, G. M., & Boore, D.M. (2006). Earthquake ground-motion prediction equations for eastern North America. *Bulletin of the Seismological Society of America, 96(6),* 2181–2205. https://doi.org/10.1785/0120050245

Atkinson, G. M., & Boore, D.M. (2014). The attenuation of Fourier amplitudes for rock sites in eastern north America. *Bulletin of the Seismological Society of America, 104(1),* 513–528. https://doi.org/10.1785/0120130136

Atkinson, G. M., & Silva, W. (2000). Stochastic modeling of California ground motions. *Bulletin of the Seismological Society of America, 90,* 255–274. https://doi.org/10.1785/0119990064

Beresnev, I., & Atkinson, G.M. (1998). FINSIM: A FORTRAN program for simulating stochastic acceleration time histories from finite faults. *Seismological Research Letters, 69(1),* 27–32. https://doi.org/10.1785/gssrl.69.1.27

Boore, D. M. (1983). Stochastic simulation of high-frequency ground motions based on seismological models of the radiated spectra. *Bulletin of the Seismological Society of America, 73(6A),* 1865–1894.

Boore, D. M. (2003). Simulation of ground motion using the stochastic method. *Pure and Applied Geophysics, 160,* 635–676. https://doi.org/10.1007/PL00012553

Boore, D. M. (2009a). Comparing stochastic point-source and finite-source ground-motion simulations: SMSIM and EXSIM. *Bulletin of the Seismological Society of America, 99(6),* 3202–3216. https://doi.org/10.1785/0120090056

Boore, D.M. (2009b). *TSPP---A collection of FORTRAN program for processing and manipulating time series* (Open-File Report 2008-1111, ver2.0). Reston, VI: U.S. Geological Survey.

Boore, D.M., & Bommer, J.J. (2005). Processing of strong-motion accelerograms: needs, options and consequences. *Soil Dynamics and Earthquake Engineering, 25(2),* 93–115. https://doi.org/10.1016/j.soildyn.2004.10.007

Boore, D. M., Skarlatoudis, A., Margaris, B., Papazachos, C., & Ventouzi, C. (2009). Along-arc and back-arc attenuation, site response, and source spectrum for the intermediate-depth 8 January 2006 M 6.7 Kyther, Greece, earthquake. *Bulletin of the Seismological Society of America, 99(4),* 2410–2434. https://doi.org/10.1785/0120080229

Boore, D.M., Stewart, J.P., Seyhan, E., & Atkinson, G.M. (2014). NGA-West2 equations for predicting PGA, PGV, and 5% damped PSA for shallow crustal earthquakes. *Earthquake Spectra, 30,* 1057–1085. https://doi.org/10.1193/070113EQS184M

Boore, D. M., Thompson, E.M., & Cadet, H. (2011). Regional correlations of V_{S30} and velocities averaged over depths less than and greater than 30 meters. *Bulletin of the Seismological Society of America, 101(6),* 3046-3059. https://doi.org/10.1785/0120110071

Borcherdt, R.D. (1992). *Simplified site classes and empirical amplification factors for site dependent code provisions, NCEER, SEAOC, BSSC.* Paper presented at workshop on site

response during earthquakes and seismic code provisions proceedings, University Southern California, Los Angeles, CA, Nov 18–20, 1992.

Brune, J. N. (1970). Tectonic stress and the spectra of seismic shear waves from earthquakes. *Journal of Geophysical Research, 75(26),* 4997–5009. https://doi.org/10.1029/JB075i026p04997

Cadet, H., Bard, P.Y., & Rodriguez-Marek A. (2012). Site effect assessment using KiK-net data: Part 1. A simple correction procedure for surface/downhole spectral ratios. *Bulletin of Earthquake Engineering, 10,* 421–448. https://doi.org/10.1007/s10518-011-9283-1

Chiou, B., Darragh, R., Gregor, N., & Silva, W. (2008). An overview of the NGA database, *Earthquake Spectra, 24(1),* 23–44. https://doi.org/10.1193/1.2894833

Darragh, B., Silva, W., & Gregor, N. (2004). *Strong motion record processing procedures for the PEER center,* Paper presented at proceedings of COSMOS workshop on strong-motion record processing, Richmond, California, May 26–27, 1–12.

Diao, H., Miyake, H., & Koketsu, K. (2018). Near-fault broad band ground-motion simulations of the 2016 Meinong, Taiwan, earthquake. *Bulletin of the Seismological Society of America, 108(6),* 3336–3357. https://doi.org/10.1785/0120180113

Douglas, J. (2003). What is a poor quality strong-motion record? *Bulletin of Earthquake Engineering, 1,* 141–156. https://doi.org/10.1023/A:1024861528201

Fukuyama, E., Ishida, M., Dreger, D.S., & Kawai, H. (1998). Automated seismic moment tensor determination by using on-line broadband seismic waveforms. *Journal of the Seismology Society of Japan, 51(1),* 149–156. https://doi.org/10.4294/zisin1948.51.1_149 (in Japanese with English abstract)

Ghasemi, H., Fukushima, Y., Koketsu, K., Miyake, H., Wang, Z., & Anderson, J.G. (2010). Ground motion simulation for the 2008 Wenchuan, China, earthquake using the stochastic finite-fault method. *Bulletin of the Seismological Society of America, 100(5B),* 2476–2490. https://doi.org/10.1785/0120090258

Ghofrani, H., & Atkinson, G. (2011). Forearc versus backarc attenuation of earthquake ground motion. *Bulletin of the Seismological Society of America, 101(6),* 3032–3045. https://doi.org/10.1785/0120110067

Ghofrani, H., & Atkinson, G. (2015). Duration of the 2011 Tohoku earthquake ground motions. *Journal of Seismology, 19,* 9-25. https://doi.org/10.1007/s10950-014-9447-y

Ghofrani, H., Atkinson, G., Goda, K., & Assatourians, K. (2013). Stochastic finite-fault simulations of the 2011 Tohoku, Japan, earthquake. *Bulletin of the Seismological Society of America, 103(2B),* 1307–1320. https://doi.org/10.1785/0120120228

Graves, R. W., Aagaard, B. T., Hudnut, K.W., Star, L. M., Stewart, J. P., & Jordan, T.H. (2008). Broadband simulations for Mw 7.8 southern San Andreas earthquakes: Ground motion sensitivity to rupture speed. *Geophysical Research Letter, 35(22),* L22302. https://doi.org/10.1029/2008GL035750

Hanks, T. C., & Kanamori, H. (1979). A Moment Magnitude Scale. *Journal of Geophysical Research, 84(B5),* 2348–2350. https://doi.org/10.1029/JB084iB05p02348

Hartzell, S. H. (1978). Earthquake aftershocks as Green's functions, *Geophysical Research Letter, 5(1),* 1–4. https://doi.org/10.1029/GL005i001p00001

Irikura, K. (1983). Semi-empirical estimation of strong ground motions during large earthquakes. *Bulletin of the Disaster Prevention Research Institute of Kyoto University, 33(2),* 63-104.

Irikura, K. (1986). *Prediction of strong acceleration motion using empirical Green's function.* Paper presented at Proceedings of the 7th Japan Earthquake Engineering. Symposium, Tokyo, Japan.

Kamagata, S., & Takewaki, I. (2017). Occurrence Mechanism of Large Acceleration in KiK-net Seismic Records during Iwate–Miyagi Nairiku Earthquake in 2008. *Frontiers in Built Environment, 3(13),* 1-18. https://doi.org/10.3389/fbuil.2017.00013

Kamae, K., Irikura, K., & Pitarka, A. (1998). A technique for simulating strong ground motion using Hybrid Green's function. *Bulletin of the Seismological Society of America, 88(2),* 357–367.

Kazama, M., Kataoka, S., & Uzuoka, R. (2012). Volcanic mountain area disaster caused by the Iwate–Miyagi NairikuEarthquake of 2008, *Japan. Soils and Foundations, 52(1),* 168–184. https://doi.org/10.1016/j.sandf.2012.01.003

Konno, K., & Ohmachi, T. (1998). Ground motion characteristics estimated from spectral ratio between horizontal and vertical components of microtremor. *Bulletin of the Seismological Society of America, 88(1),* 228–241.

Mavroeidis, G. P., & Papageorgiou, A. S. (2003). A mathematical representation of near-fault ground motions. *Bulletin of the Seismological Society of America, 93(3),* 1099–1131. https://doi.org/10.1785/0120020100

Motazedian, D. (2006). Region-specific key seismic parameters for earthquakes in Northern Iran. *Bulletin of the Seismological Society of America, 96(4A),* 1383–1395. https://doi.org/10.1785/0120050162

Motazedian, D., & Atkinson, G. M. (2005). Stochastic finite-fault modeling based on a dynamic corner frequency. *Bulletin of the Seismological Society of America, 95(3),* 995–1010. https://doi.org/10.1785/0120030207

Motazedian, D., & Moinfar, A. (2006). Hybrid stochastic finite fault modeling of 2003, M 6.5, Bam earthquake (Iran). *Journal of Seismology, 10,* 91–103. https://doi.org/10.1007/s10950-005-9003-x

Pitarka, A., Somerville, P., Fukushima, Y., Uetake, T., & Irikura, K. (2000). Simulation of near-fault strong-ground motion using hybrid green's functions. *Bulletin of the Seismological Society of America,90(3),* 566–586. https://doi.org/10.1785/0119990108

Safak, E. (1991). *Problems with using spectral ratios to estimate site amplification*. Paper presented at 4th international conference on seismic zonation, vol II. EERI, Oakland, pp 277–284.

Steidl, J. H. (1993). Variation of site response at the UCSB dense array of portable accelerometers. *Earthquake Spectra, 9,* 289–3020. https://doi.org/10.1193/1.1585716

Steidl, J. H., Tumarkin, A. G., & Archuleta, R. J. (1996). What is a reference site?. *Bulletin of the Seismological Society of America, 86(6),* 1733–1748.

Sugimura, A. (1960). Zonal arrangement of some geophysical and petrological features in Japan and its environs. *Jornal of Faculty of Science, University of Tokyo, 12(2),* 133–153.

Suzuki, W., Aoi, S., & Sekiguchi, H. (2010). Rupture process of the 2008 Iwate–Miyagi Nairiku, Japan, earthquake derived from near-source strong-motion records. *Bulletin of the Seismological Society of America, 100(1),* 256-266. http://dx.doi.org/10.1785/0120090043

Ugurhan, B., Askan, A., Akinci, A., & Malagnini, L. (2012). Strong-ground-motion simulation of the 6 April 2009 L'Aquila, Italy, earthquake. *Bulletin of the Seismological Society of America, 102(4),* 1429–1445. https://doi.org/10.1785/0120110060

Van Houtte, C., Drouet, S., & Cotton, F. (2011). Analysis of the origins of κ (Kappa) to compute hard rock to rock adjustment factors for GMPEs. *Bulletin of the Seismological Society of America, 101(6),* 2926–2941. https://doi.org/10.1785/0120100345

Wessel, P., & Smith, W. H. F. (1991). Free software helps map and display data. *Eos, Transactions American Geophysical Union, 72(41),* 441. https://doi.org/10.1029/90EO00319

Zhang, L., Chen, G., & Jiang, H. (2016). Stochastic ground-motion simulations for the 2016 Kumamoto, Japan, Earthquake. *Earth, Planets and Space, 68(184),* 1-13. https://doi.org/10.1186/s40623-016-0565-3

747 **Table 1.** Input parameters for finite-fault stochastic simulation of the 2008 Iwate-Miyagi
748 earthquake
749

Parameters	Model 1[a]	Model 2[b]	Model 3[c]
Source			
Moment magnitude	6.9	6.9	6.9
strike & dip	209°, 40°	209°, 40°	209°, 51°
Length, width and depth	40, 18, 6.5 km	40, 18, 6.5 km	38, 18, 7.8 km
Depth to top of fault plane	0.7 km	0.7 km	0.8 km
Sub-fault dimensions	2×2 km	2×2 km	2×2 km
Stress drop, $\Delta\sigma$	160 bars	160 bars	160 bars
Slip distribution	prescribed	random	prescribed
Percentage pulsing area	50%	50%	50%
Shear wave velocity, β	3.6 km/s	3.6 km/s	3.6 km/s
Density, ρ	2.8 gr/cm^3	2.8 gr/cm^3	2.8 gr/cm^3
Rupture velocity	0.5 β	0.5 β	0.67 β
Path[d]			
Geometrical spreading, Z(R)	$R^{-1.0}$, R<50 km $50\,R^{-0.5}$, R≥ 50 km	$R^{-1.0}$, R<50 km $50\,R^{-0.5}$, R≥ 50 km	$R^{-1.0}$, R<50 km $50\,R^{-0.5}$, R≥ 50 km
Quality factor, Q(f)	$Q(f)= 294\,f^{0.45}$ (fore-arc) $Q(f) = 180\,f^{0.44}$ (back-arc)	$Q(f)= 294\,f^{0.45}$ (fore-arc) $Q(f) = 180\,f^{0.44}$ (back-arc)	$Q(f)= 294\,f^{0.45}$ (fore-arc) $Q(f) = 180\,f^{0.44}$ (back-arc)
Path duration (sec)	0.0, R=0.0 km 13.09, R=70.0 km 11.68, R=140 km 35.09, R=240 km	0.0, R=0.0 km 13.09, R=70.0 km 11.68, R=140 km 35.09, R=240 km	0.0, R=0.0 km 13.09, R=70.0 km 11.68, R=140 km 35.09, R=240 km
Site[d]			
Amplification	SBRc and QWL	SBRc and QWL	SBRc and QWL
Zero-distance kappa, κ_0	0.0473 s	0.0473 s	0.0473 s

750 [a] Source parameters by Suzuki et al. (2010). [b] Source parameters by Suzuki et al. (2010), but with a random slip
751 distribution. [c] Source parameters by Asano and Iwata (2011). [d] Path and site parameters were computed in this study.
752

753

754 **Table 2.** Absolute residuals and standard deviation of three defined models

Static Parameter	Model 1	Model 2	Model 3
std	0.122	0.120	0.122
$\overline{\lvert res \rvert}$	0.182	0.177	0.183

755

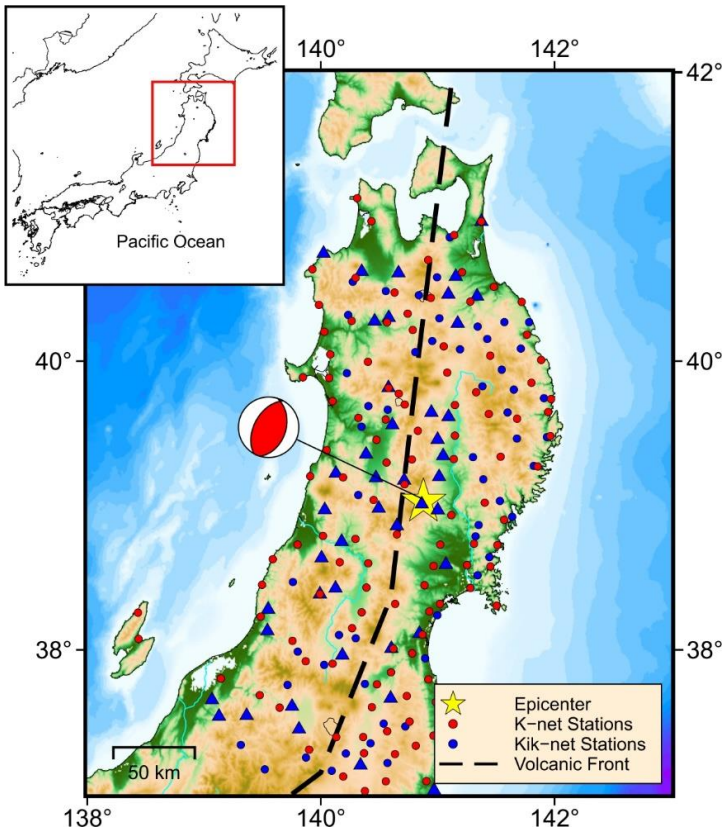

Figure 1. The spatial distribution of K-Net (red circles) and Kik-net (blue circles) stations at closest distance from the fault plane up to 220 km. Blue triangles depict the Kik-net stations for which the simulations are performed. The epicenter and focal mechanism of the event are shown by yellow star and red beach ball, repectively. Black dashed line shows the volcanic front. The right and left sides of the volcanic front are fore-arc and back-arc regions, respectively.

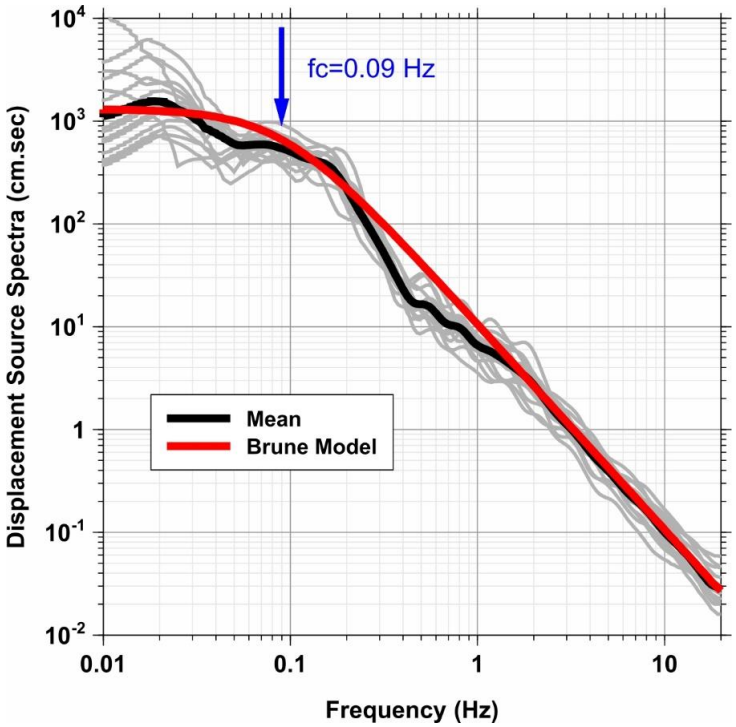

Figure 2. Displacement source spectra of borehole records from Kik-net stations (grey curves) with shear-wave velocity exceeding 2000 m/s, source spectra mean (black curve) and best fitted Brune's model (red curve). The displacement source spectra for each station was obtained by removing the path effects including geometrical spreading and quality factor from Fourier displacement spectra.

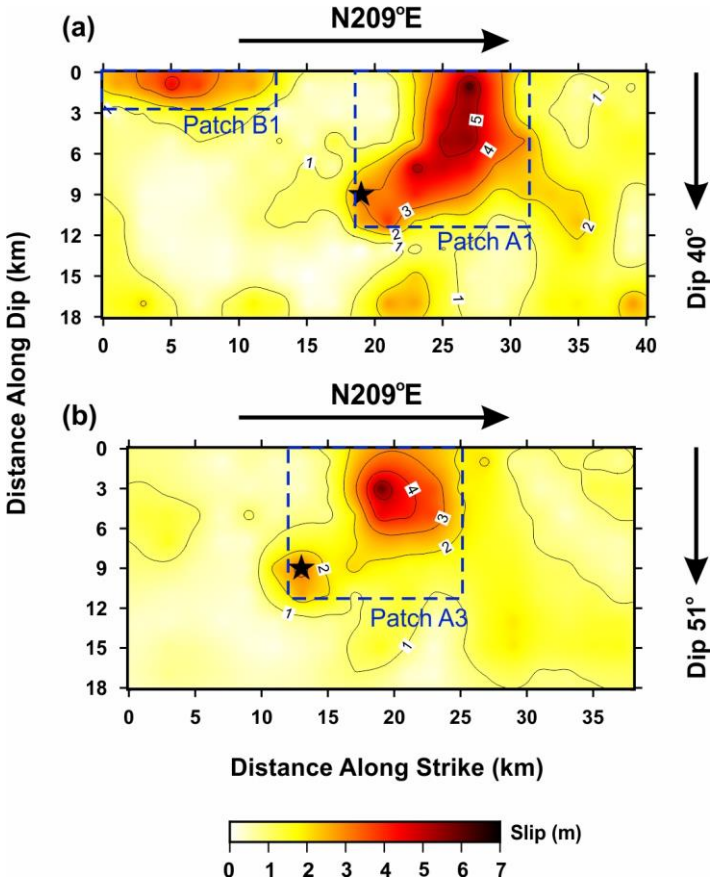

Figure 3. Prescribed slip distributions used in simulations. (a) Model 1: fault geometry and slip distribution provided by Suzuki et al. (2010), (b) Model 3: fault geometry and slip distribution obtained by Asano and Iwata (2011). The color bar indicates the slip value within the fault plane. Dashed blue rectangles represent the slip patches which affect recorded strong motions in near-field stations. Note: these patches are different from asperity definitions.

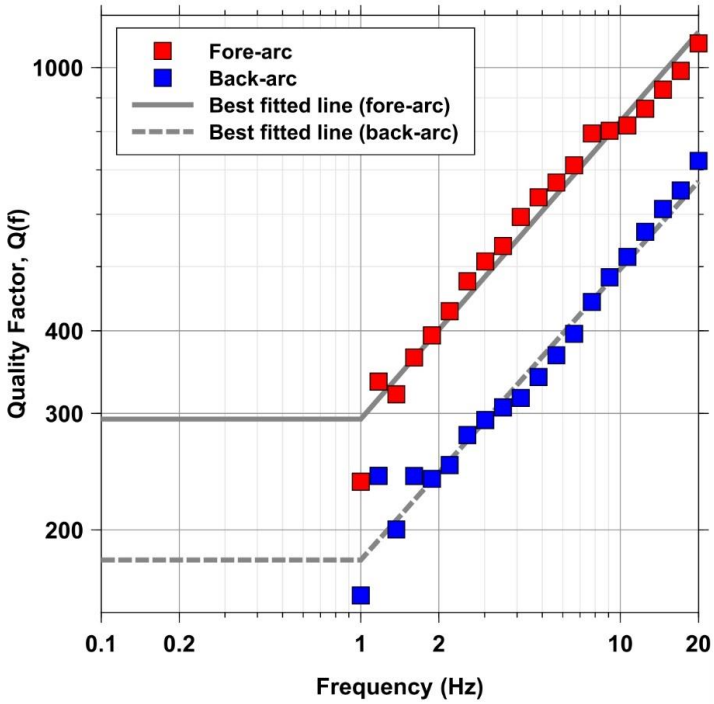

Figure 4. Quality factor for fore-arc (red square) and back-arc (blue square) regions. Solid and dashed grey lines show the best fitted lines on the observed data for fore-arc and back-arc, respectively. Given that the attenuation is inversely related to the quality factor, stations located in the back-arc region experience larger attenuation than the fore-arc.

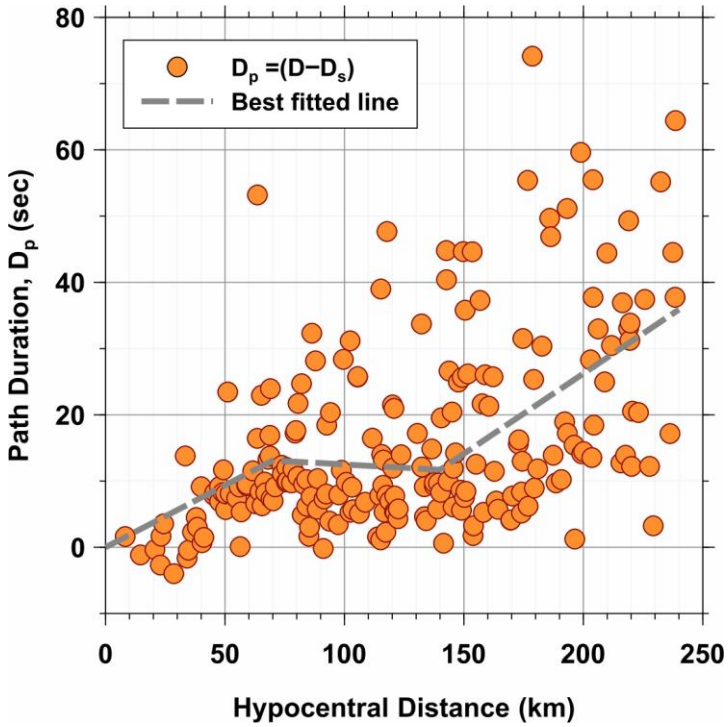

Figure 5. Path duration (D_P) model used in the simulations. Orange circles and dashed grey line show the observed path duration for each station and best regressed line on the observed data, respectively. The path duration was calculated by subtracting the source duration (D_S) from the total duration (D). In this study, proposed model by Boore and Thompson (2014) was used to compute total duration. Also the source duration was considered to be the inverse of static corner frequency.

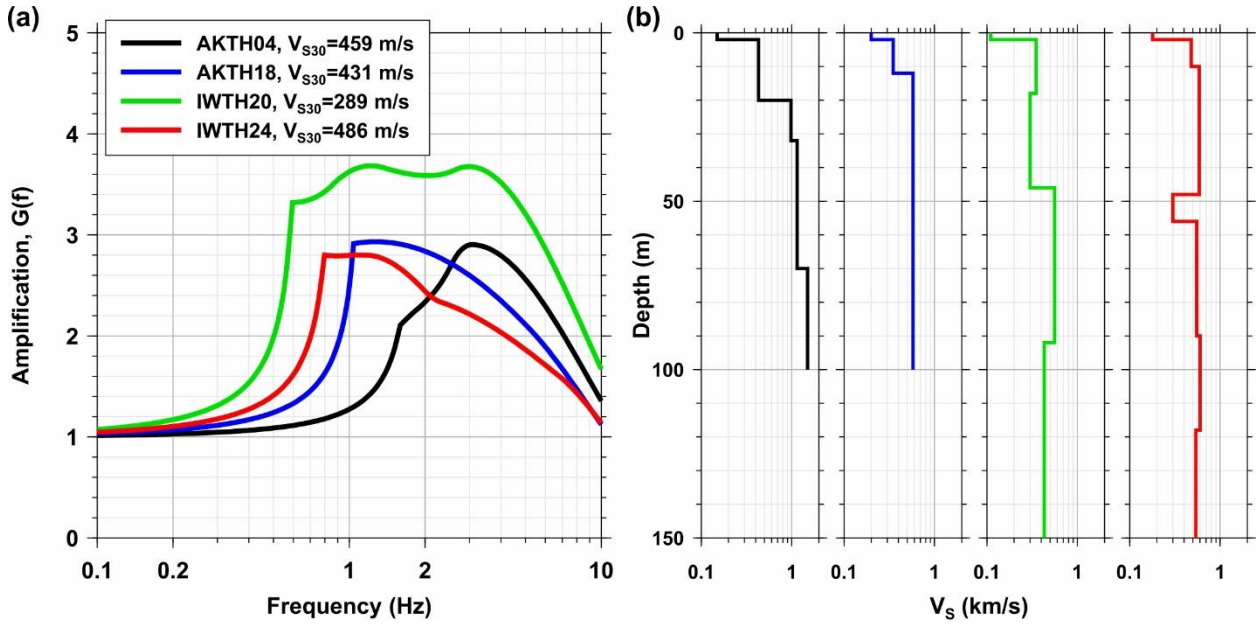

Figure 6. (a) Site response obtained from the quarter wavelength (QWL) method for AKTH04 (black curve), AKTH18 (blue curve), IWTH20 (green curve) and IWTH24 (red curve), (b) shear-wave velocity profile related to these stations. The borehole accelerometer installation site with low shear-wave velocity at three stations (AKTH18, IWTH20 and IWTH24) cannot be interpreted as bedrock to be used in the SBR method. Therefore, the site response at these stations may be underestimated because of probable amplification of the borehole sites. Also the abnormal observed acceleration at station AKTH04 causes unreliable site amplification obtained by the SBR method.

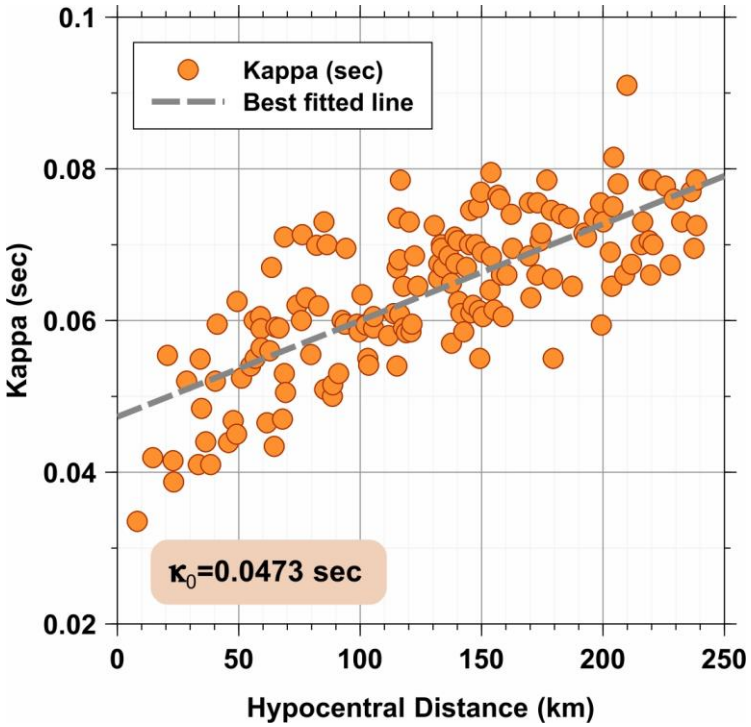

Figure 7. Estimated kappa for all surface stations. The line suggests a zero-distant of 0.0473 sec. High frequency motions are attenuated by the surface soil layers which is described using κ_0 model.

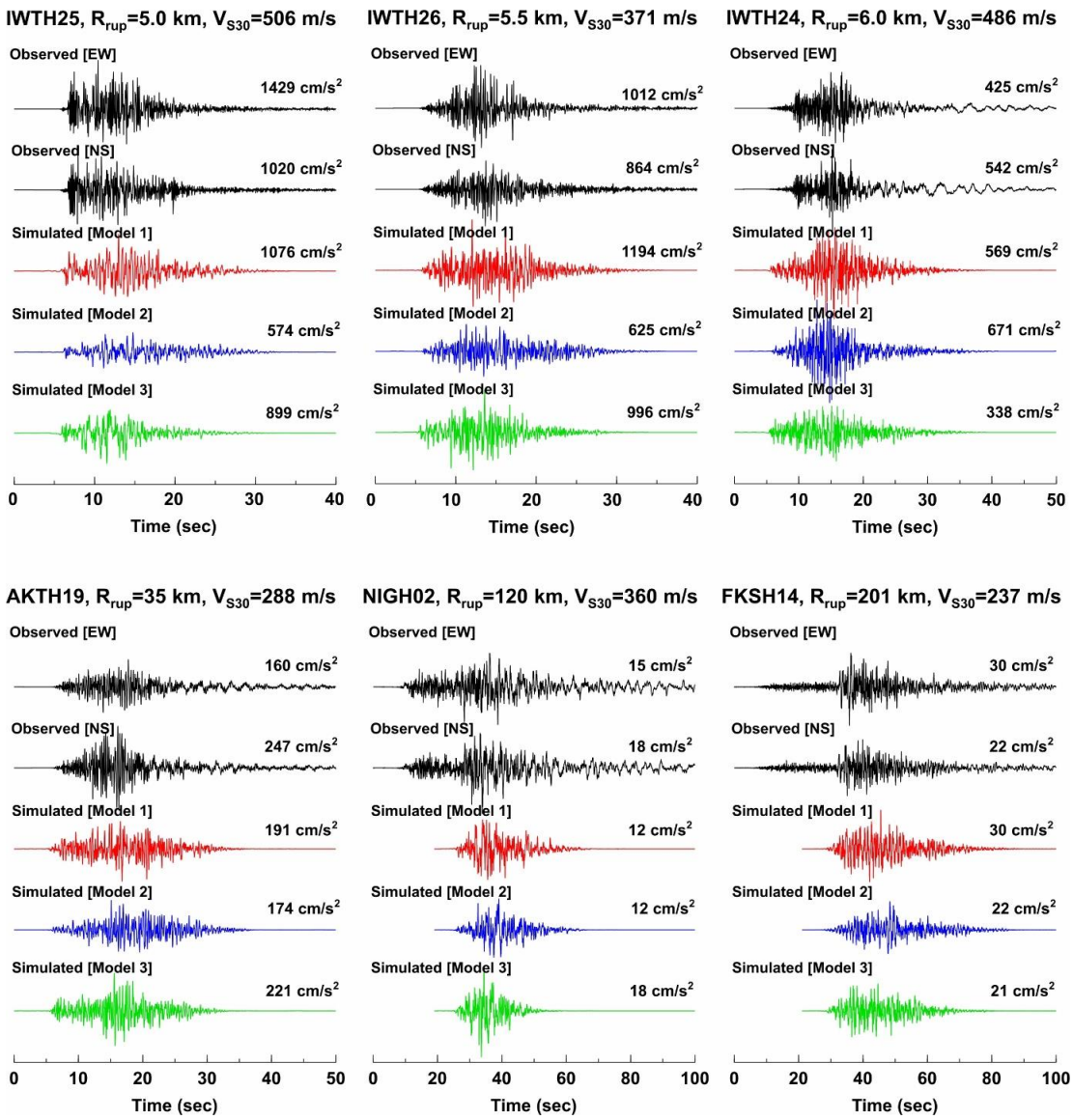

Figure 8. Comparison of the observed (black) and simulated acceleration time series by Model 1 (red), Model 2 (blue) and Model 3 (green) for the six selected stations. PGA is written at the end of each trace. We see a good correlation between the observed and simulated acceleration time series by Model 1 at all stations. Model 2 underestimates the simulated PGA at IWTH25 and IWTH26, and Model 3 cannot reflect the actual recorded accelerations at IWTH24.

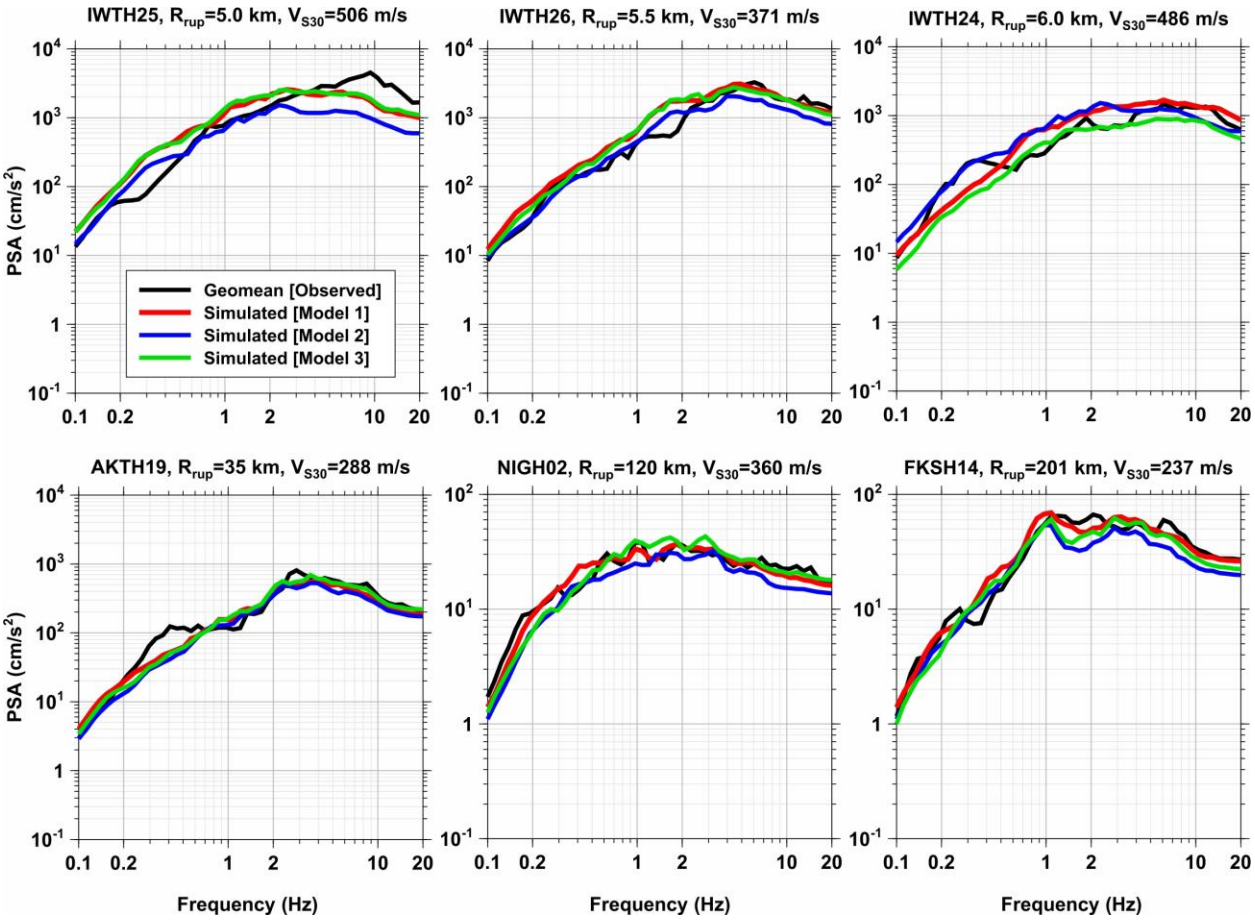

Figure 9. Comparison of the observed (black curve) and simulated 5% damped PSAs by model 1 (red curve), model 2 (blue curve) and model 3 (green curve) for the six selected stations. The observed PSAs curves are the geometric mean of the two horizontal components (EW and NS). For all stations, a good match between the observed and simulated PSAs by Model 1 is clear at all frequencies. The simulated PSAs by Model 2 are lower than the observed ones at IWTH25 and IWTH26 especially at high frequencies. This underestimation is also observed for the simulated PSA by Model 3 at station IWTH24.

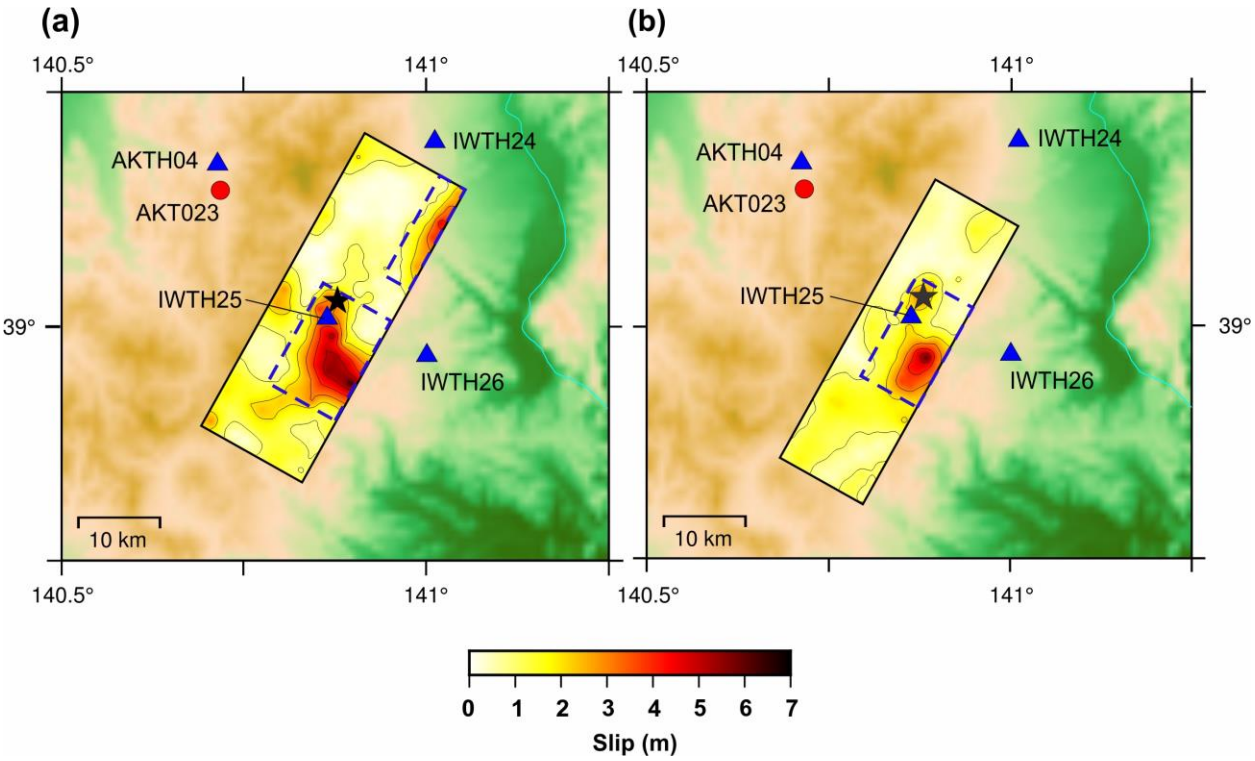

Figure 10. Surface projection of the slip distribution for (a) Model 1 (Suzuki et al., 2010), (b) Model 3 (Asano and Iwata, 2011). Black star and blue triangles indicate the rupture starting point and the Kik-net strong motion stations, respectively. These stations are used to describe the effect of slip distribution on the simulated results. The red circle is the nearest K-Net station (AKT023) to station AKTH04 where the large recorded accelerations are not interpreted by seismological aspects. The dashed blue rectangles represent the slip patches.

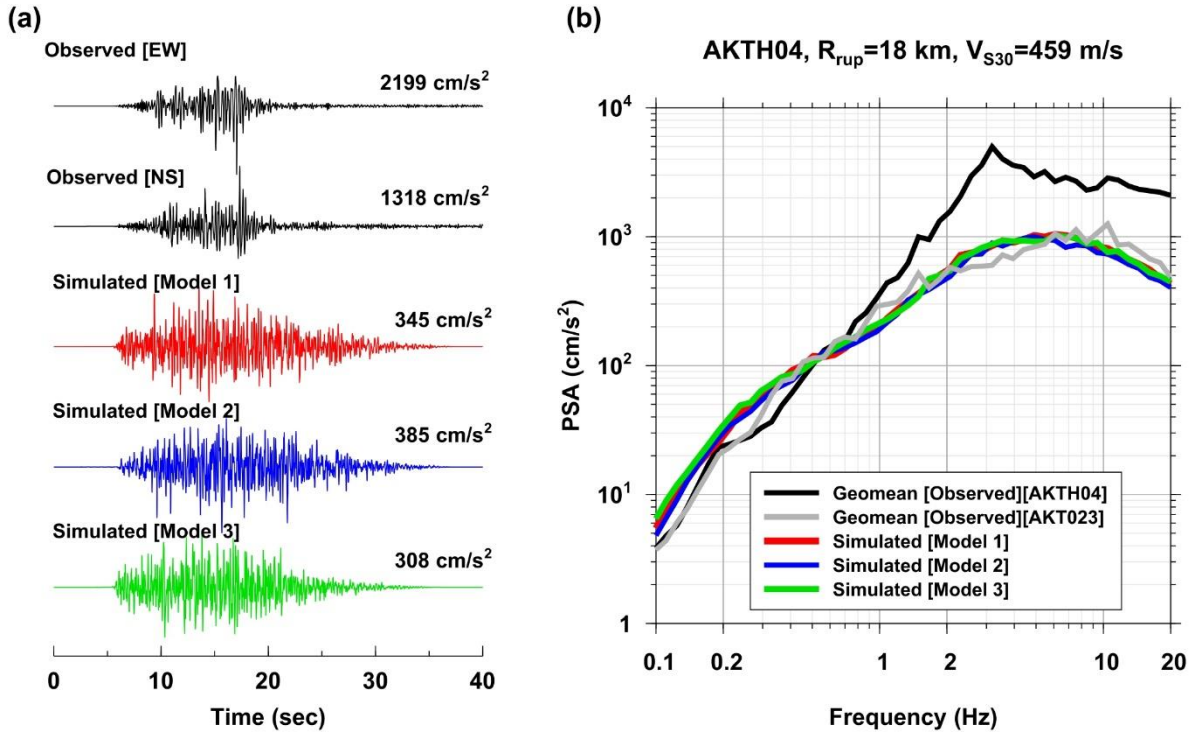

Figure 11. The simulated results for station AKTH04. Comparison of the observed and simulated (a) acceleration time series (b) 5% damped pseudo spectral acceleration (PSA). The gray curve shows the observed PSAs of geometric mean of two horizontal components at AKT023 which is the nearest station to AKTH04. The recorded acceleration at AKTH04 for non-seismological reason is very high and the simulation models successfully interpret the applied motions to the station. Note: the vertical-scale of the observed and simulated acceleration time series are different.

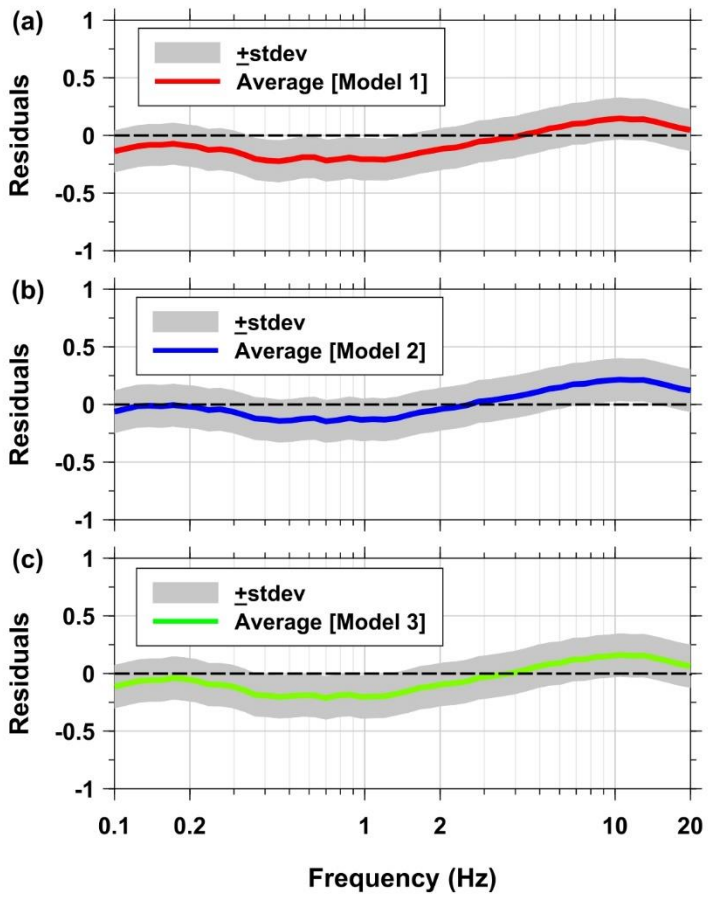

Figure 12. Calculated residuals between the observed and simulated 5% damped pseudo spectral acceleration for (a) Model 1, (b) Model 2 and (c) Model 3. The colored thick curves and the gray shaded areas show the average of the residuals and the standard deviation range, respectively. The negative values of the residual represent an overestimation by the simulation models, whereas the positive values show an underestimation.

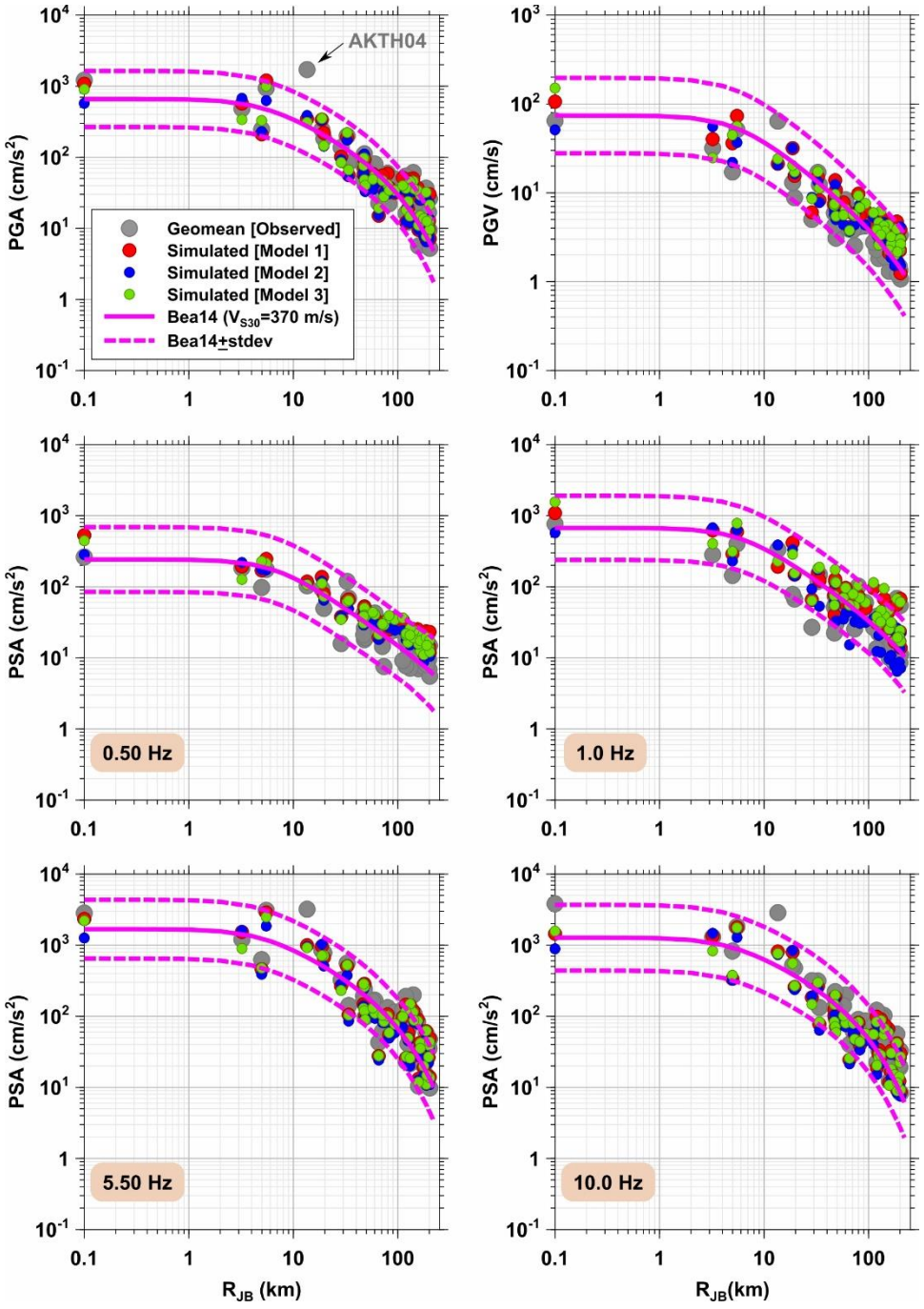

Figure 13. Comparison of the simulated, observed and predicted PGAs, PGVs and PSAs at frequencies of 0.5, 1.0, 5.5 and 10 Hz. The predicted intensity measures (pink curve) were estimated using GMPEs introduced by Boore et al. (2014). The dashed pink curves show the lower and upper bounds of standard deviation of GMPEs. The grey, red, blue and green circles represent the observed and simulated intensity measures using Model 1, Model 2 and Model 3, respectively.

Figure_1.

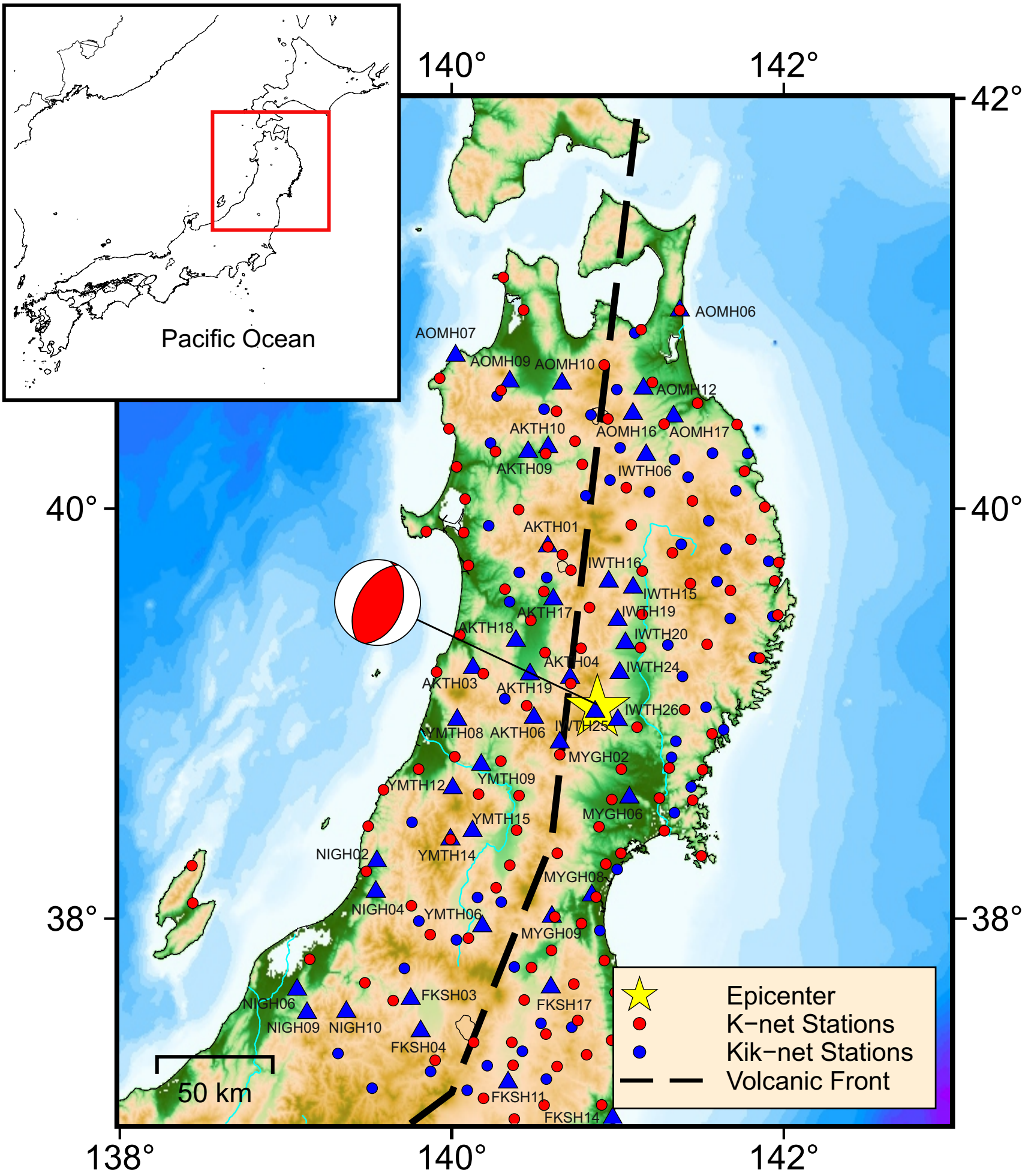
Pacific Ocean
140°
142°
42°
40°
38°
138°
AOMH06
AOMH07
AOMH09
AOMH10
AOMH12
AOMH16
AOMH17
AKTH10
AKTH09
IWTH06
AKTH01
IWTH16
IWTH15
AKTH17
IWTH19
AKTH18
IWTH20
AKTH04
IWTH24
AKTH03
AKTH19
IWTH26
YMTH08
AKTH06
IWTH25
MYGH02
YMTH09
YMTH12
MYGH06
YMTH15
NIGH02
YMTH14
MYGH08
NIGH04
YMTH06
MYGH09
FKSH03
FKSH17
NIGH06
NIGH09
NIGH10
FKSH04
FKSH11
FKSH14
50 km
Epicenter
K−net Stations
Kik−net Stations
Volcanic Front

Figure_2.

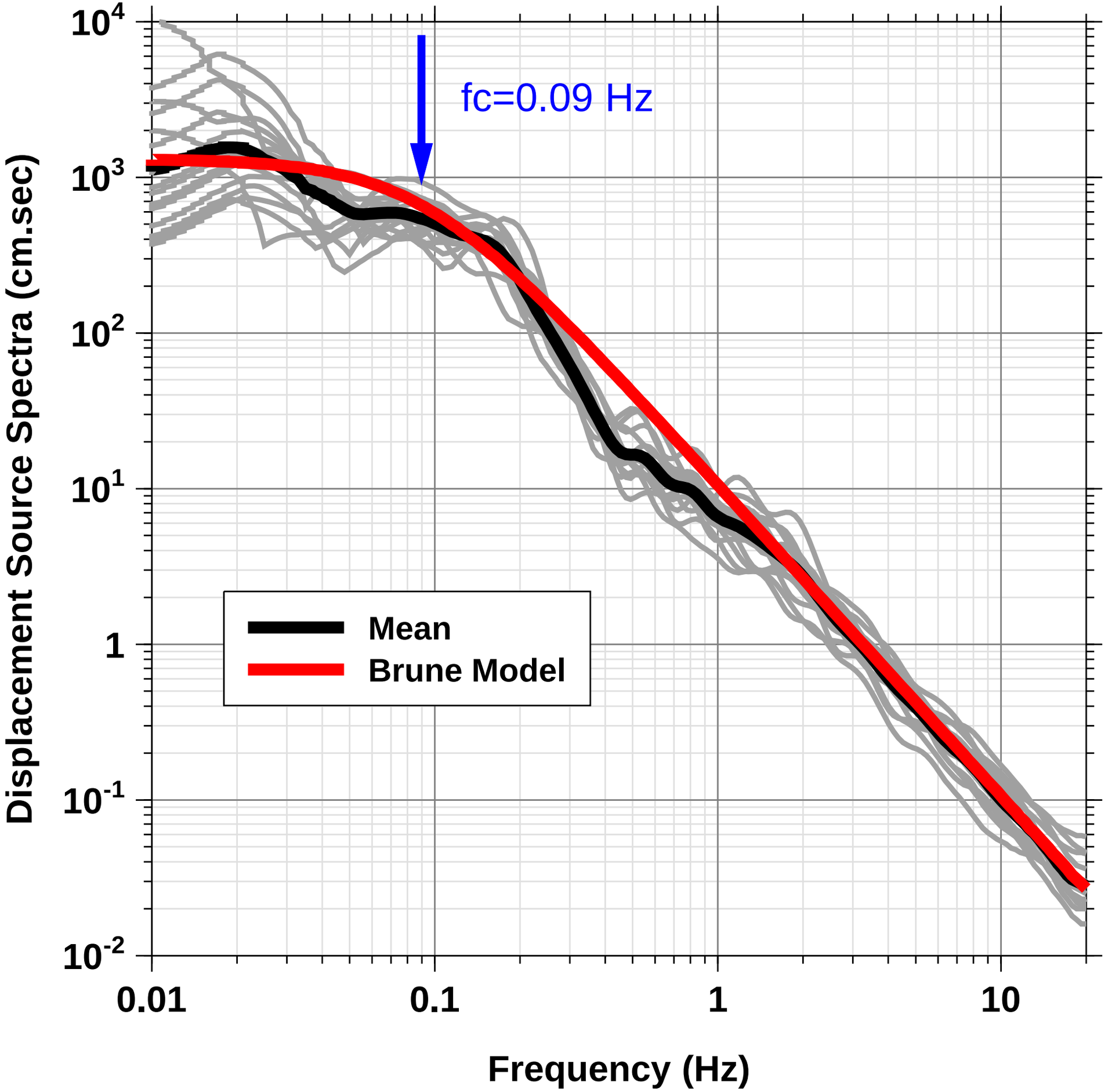
fc=0.09 Hz
Mean
Brune Model
Displacement Source Spectra (cm.sec)
Frequency (Hz)
10^4
10^3
10^2
10^1
1
10^-1
10^-2
0.01
0.1
1
10

Figure_3.

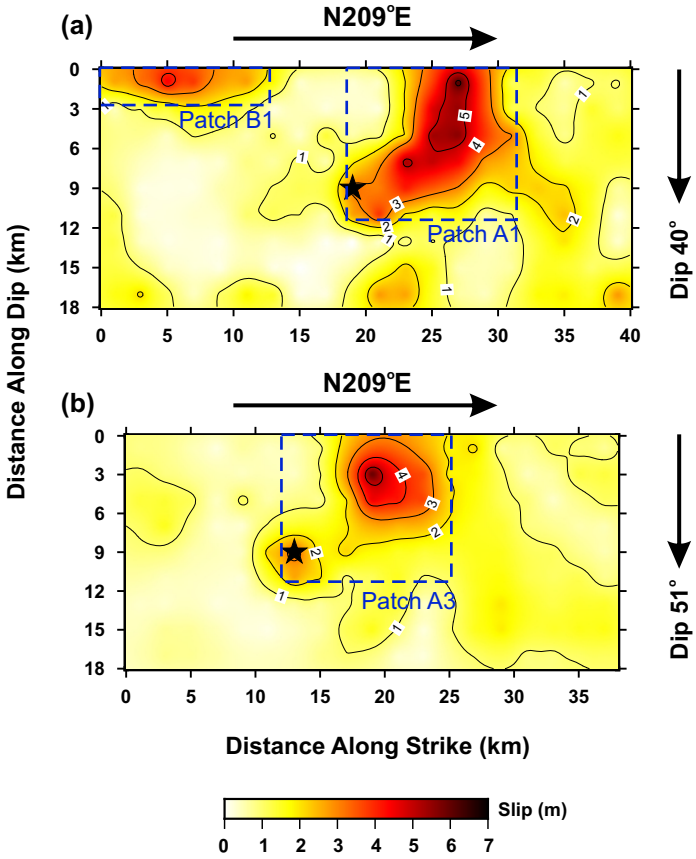
(a)
N209°E
Patch B1
Patch A1
Dip 40°
(b)
N209°E
Patch A3
Dip 51°
Distance Along Dip (km)
Distance Along Strike (km)
Slip (m)
0 1 2 3 4 5 6 7

Figure_4.

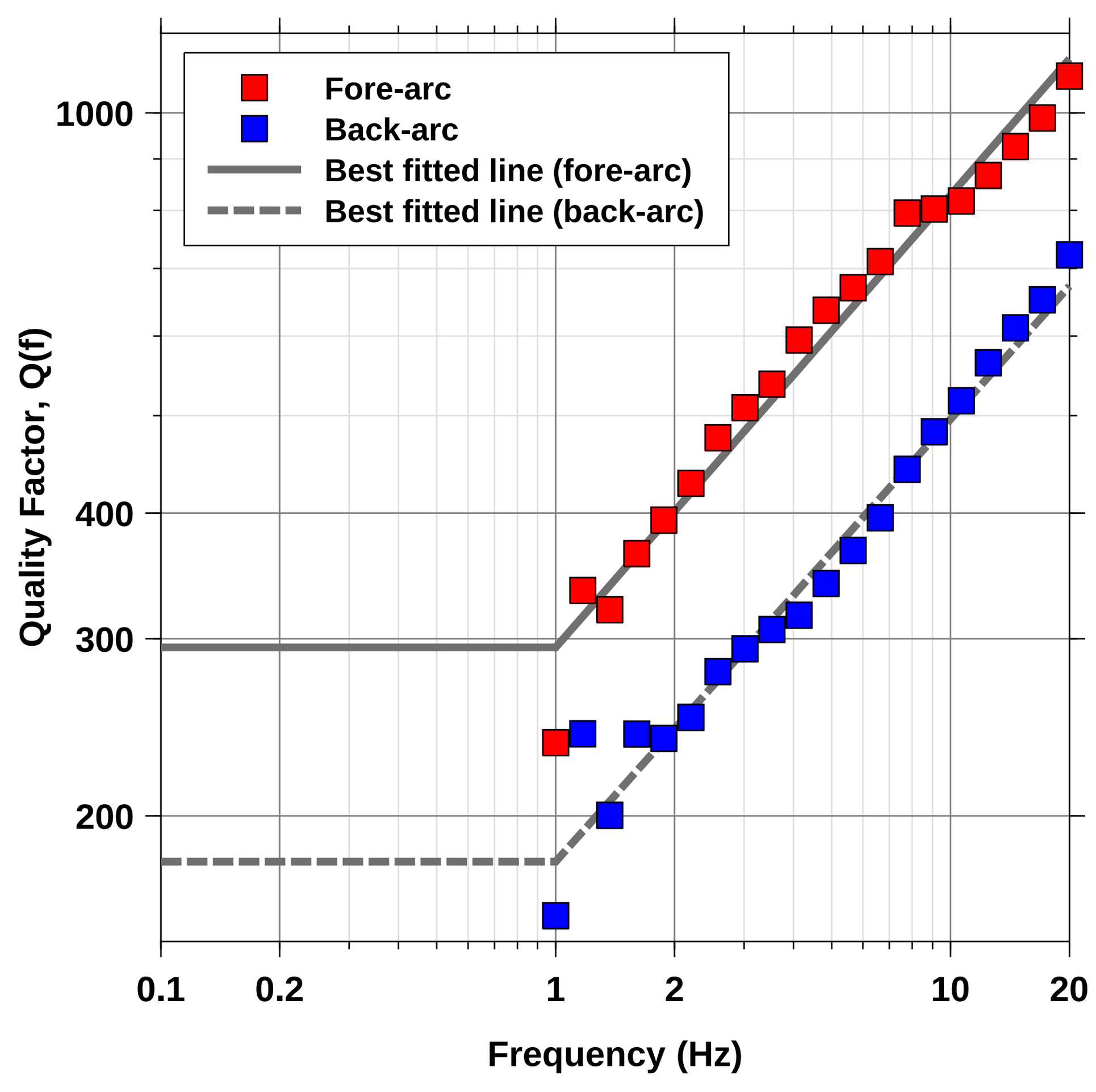
Fore-arc
Back-arc
Best fitted line (fore-arc)
Best fitted line (back-arc)
1000
400
300
200
Quality Factor, Q(f)
0.1
0.2
1
2
10
20
Frequency (Hz)

Figure_5.

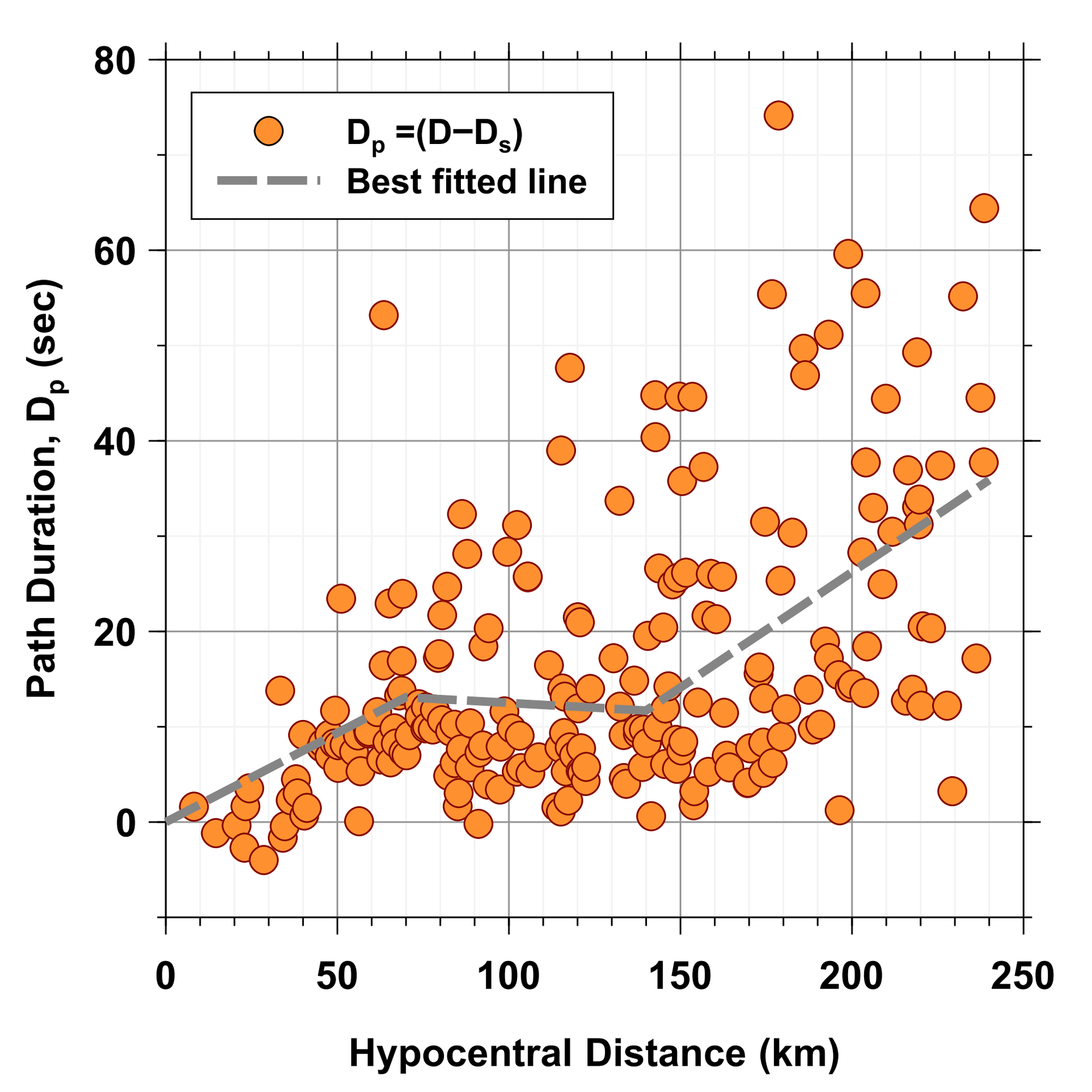
$D_p = (D - D_s)$
Best fitted line
Path Duration, D_p (sec)
Hypocentral Distance (km)
0
20
40
60
80
0
50
100
150
200
250

Figure_6.

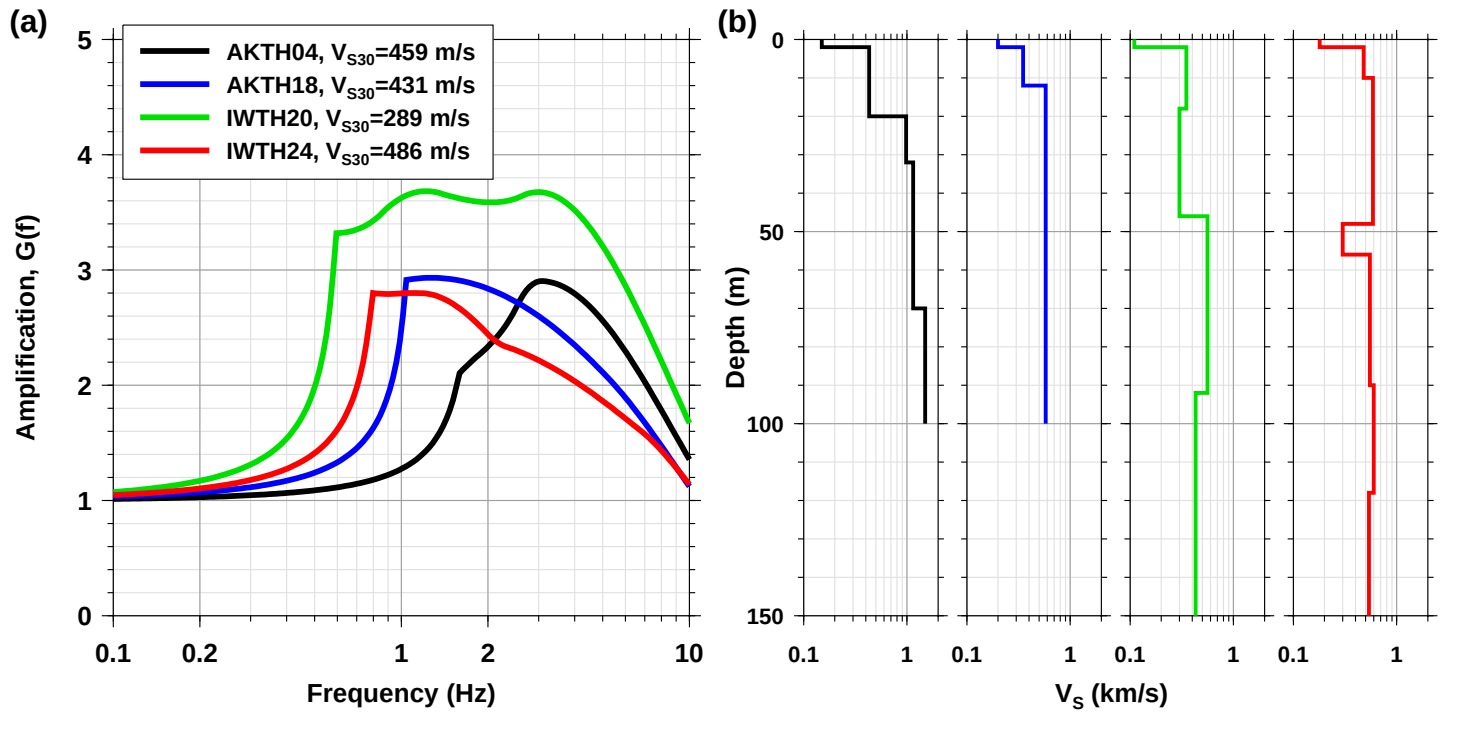
(a)
AKTH04, V_{S30}=459 m/s
AKTH18, V_{S30}=431 m/s
IWTH20, V_{S30}=289 m/s
IWTH24, V_{S30}=486 m/s
Amplification, G(f)
Frequency (Hz)
0.1
0.2
1
2
10
0
1
2
3
4
5
(b)
Depth (m)
0
50
100
150
V_S (km/s)
0.1
1

Figure_7.

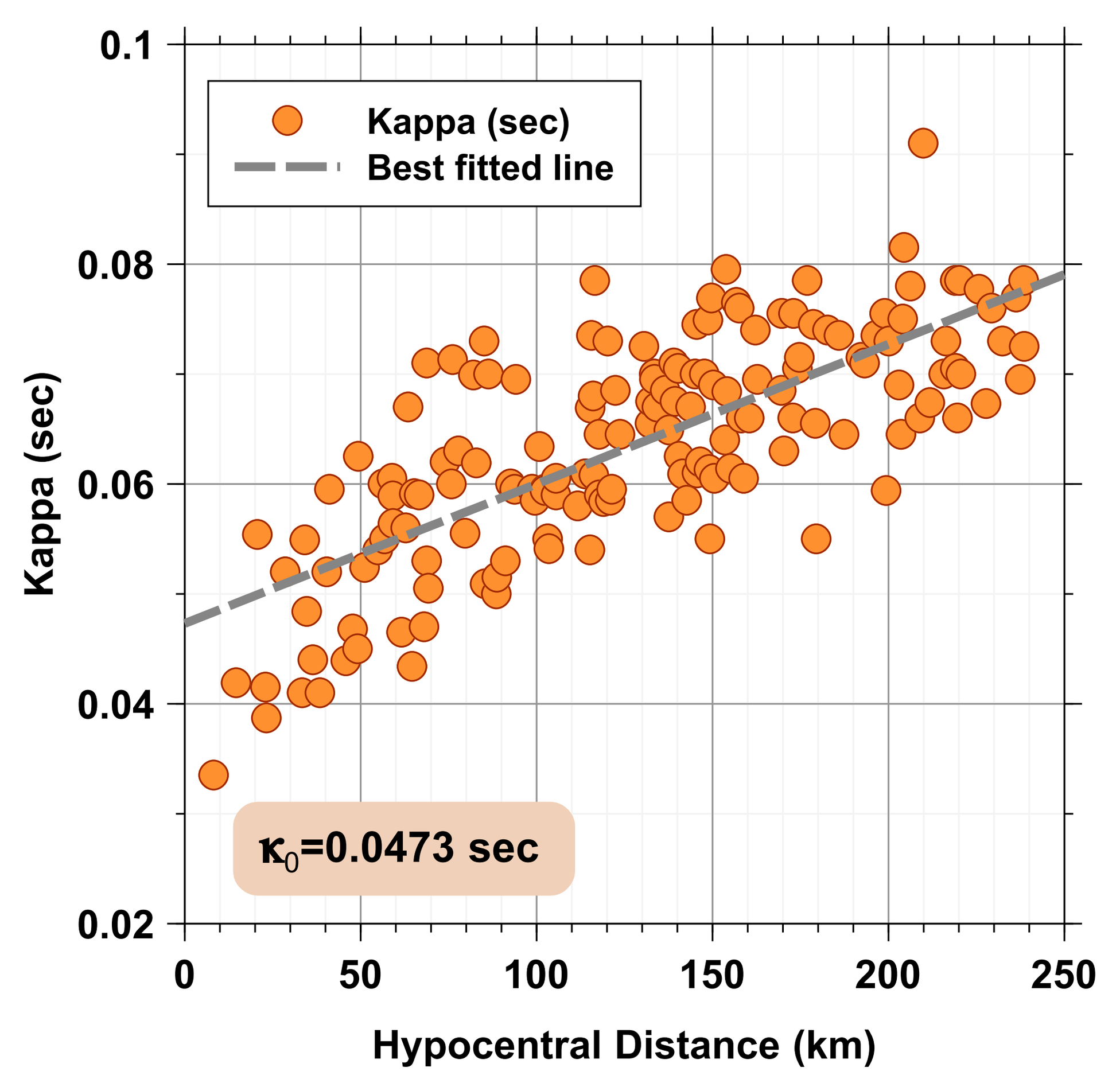
Kappa (sec)
Best fitted line
κ_0=0.0473 sec
0.1
0.08
0.06
0.04
0.02
Kappa (sec)
0
50
100
150
200
250
Hypocentral Distance (km)

Figure_8.

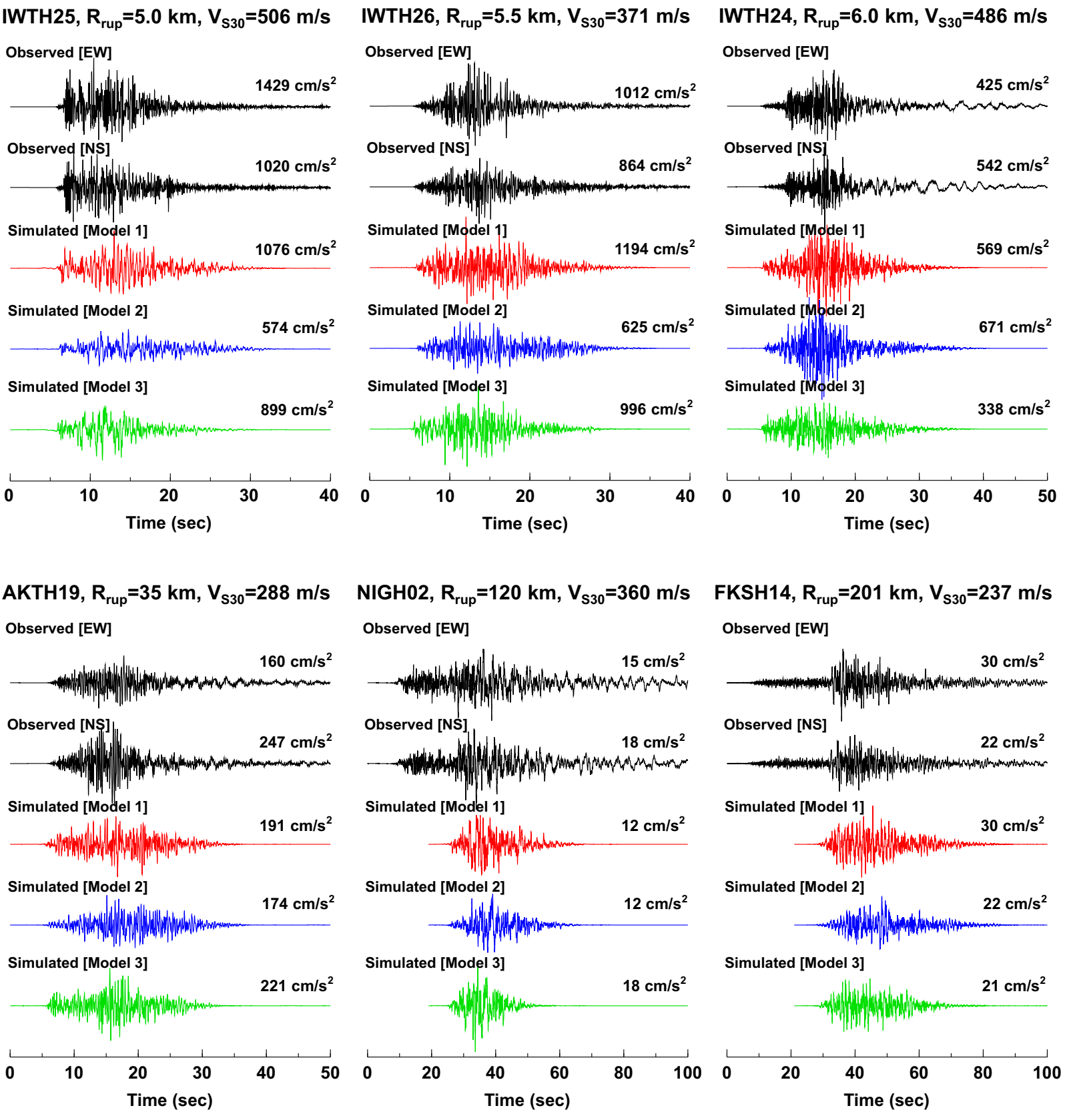
IWTH25, R_rup=5.0 km, V_S30=506 m/s
Observed [EW]
1429 cm/s²
Observed [NS]
1020 cm/s²
Simulated [Model 1]
1076 cm/s²
Simulated [Model 2]
574 cm/s²
Simulated [Model 3]
899 cm/s²
0 10 20 30 40
Time (sec)
IWTH26, R_rup=5.5 km, V_S30=371 m/s
Observed [EW]
1012 cm/s²
Observed [NS]
864 cm/s²
Simulated [Model 1]
1194 cm/s²
Simulated [Model 2]
625 cm/s²
Simulated [Model 3]
996 cm/s²
0 10 20 30 40
Time (sec)
IWTH24, R_rup=6.0 km, V_S30=486 m/s
Observed [EW]
425 cm/s²
Observed [NS]
542 cm/s²
Simulated [Model 1]
569 cm/s²
Simulated [Model 2]
671 cm/s²
Simulated [Model 3]
338 cm/s²
0 10 20 30 40 50
Time (sec)
AKTH19, R_rup=35 km, V_S30=288 m/s
Observed [EW]
160 cm/s²
Observed [NS]
247 cm/s²
Simulated [Model 1]
191 cm/s²
Simulated [Model 2]
174 cm/s²
Simulated [Model 3]
221 cm/s²
0 10 20 30 40 50
Time (sec)
NIGH02, R_rup=120 km, V_S30=360 m/s
Observed [EW]
15 cm/s²
Observed [NS]
18 cm/s²
Simulated [Model 1]
12 cm/s²
Simulated [Model 2]
12 cm/s²
Simulated [Model 3]
18 cm/s²
0 20 40 60 80 100
Time (sec)
FKSH14, R_rup=201 km, V_S30=237 m/s
Observed [EW]
30 cm/s²
Observed [NS]
22 cm/s²
Simulated [Model 1]
30 cm/s²
Simulated [Model 2]
22 cm/s²
Simulated [Model 3]
21 cm/s²
0 20 40 60 80 100
Time (sec)

Figure_9.

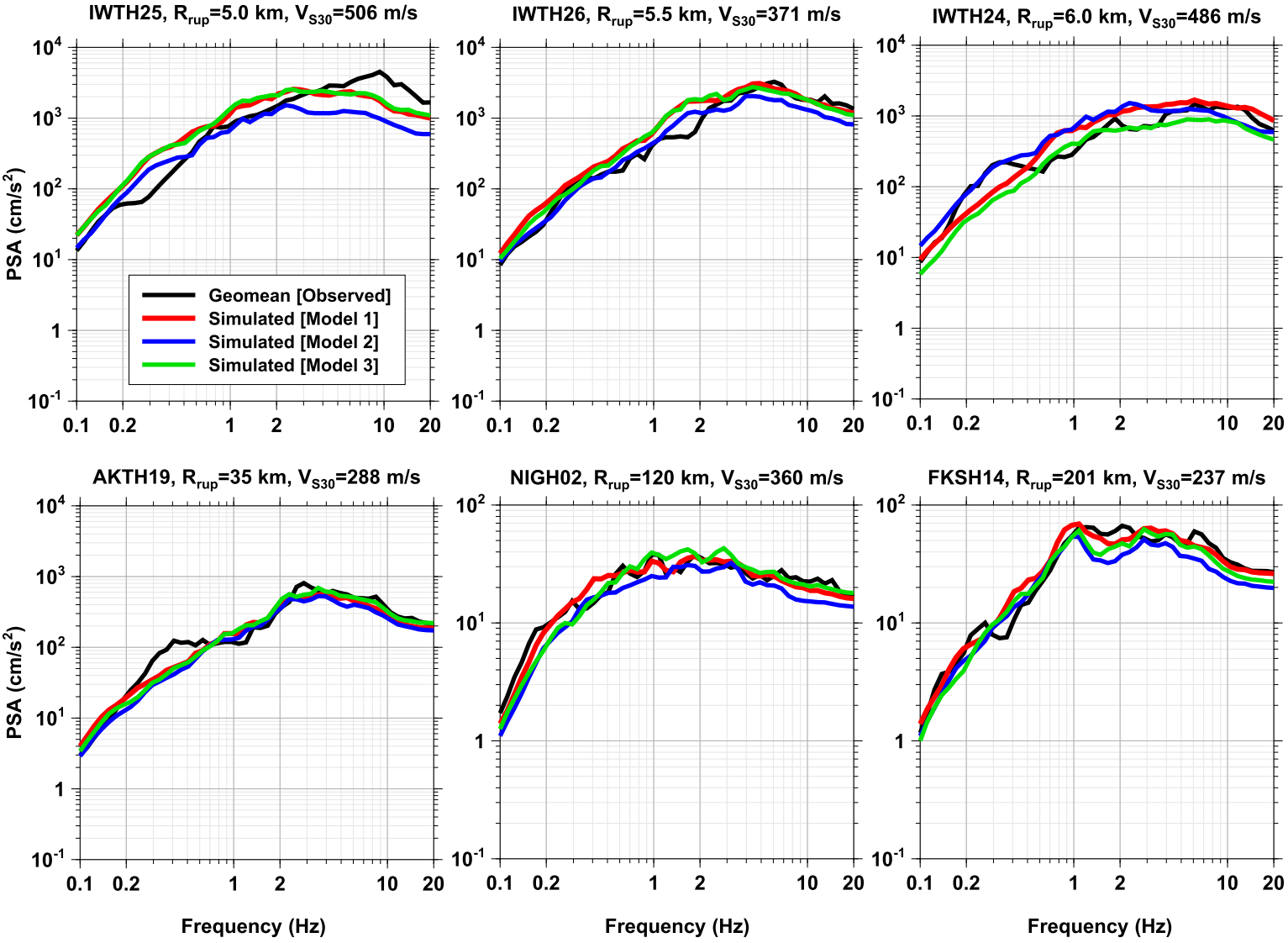
IWTH25, Rrup=5.0 km, VS30=506 m/s
IWTH26, Rrup=5.5 km, VS30=371 m/s
IWTH24, Rrup=6.0 km, VS30=486 m/s
AKTH19, Rrup=35 km, VS30=288 m/s
NIGH02, Rrup=120 km, VS30=360 m/s
FKSH14, Rrup=201 km, VS30=237 m/s
PSA (cm/s2)
Frequency (Hz)
Geomean [Observed]
Simulated [Model 1]
Simulated [Model 2]
Simulated [Model 3]

Figure_10.

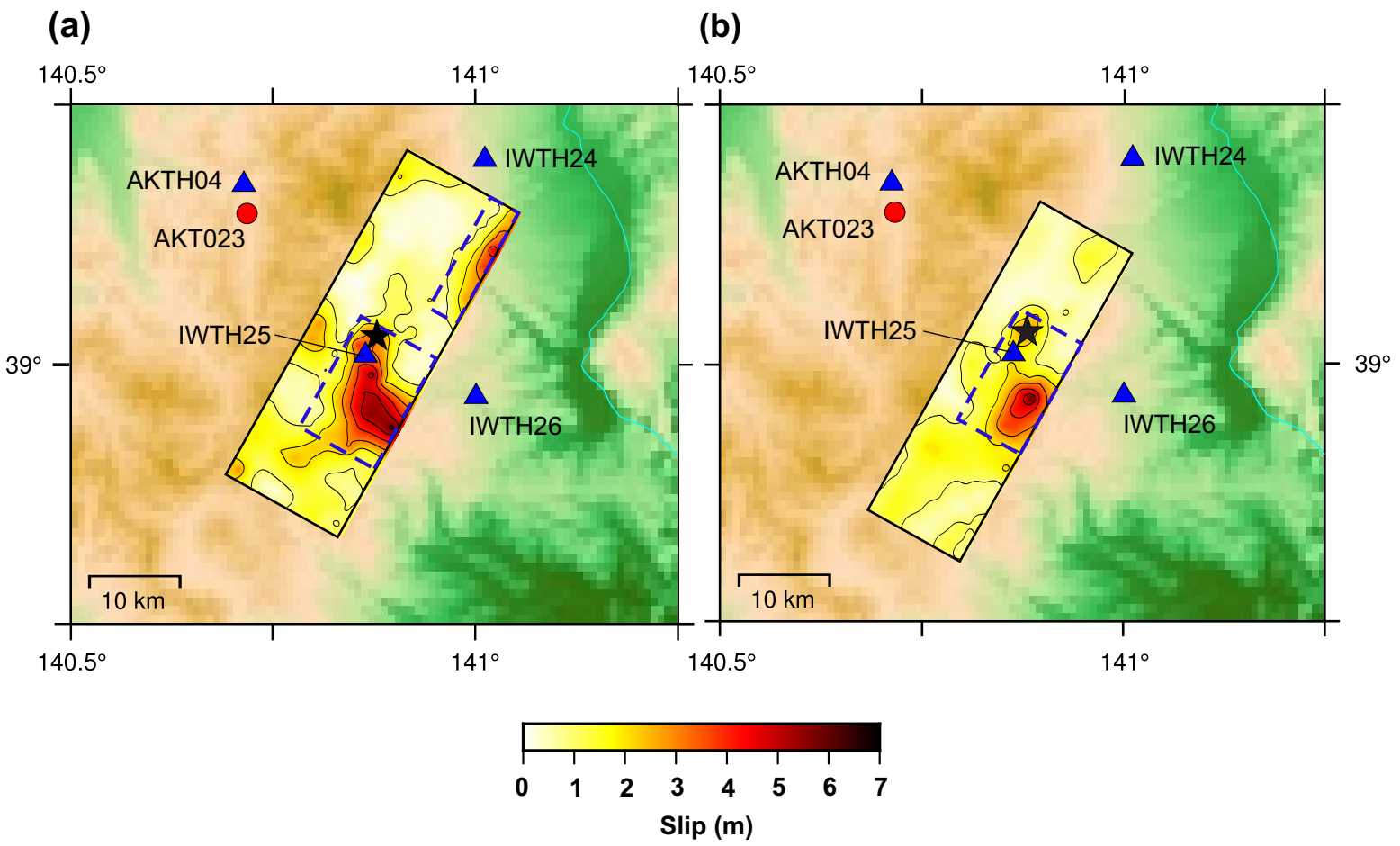
(a)
(b)
140.5°
141°
39°
AKTH04
AKT023
IWTH24
IWTH25
IWTH26
10 km
0
1
2
3
4
5
6
7
Slip (m)

Figure_11.

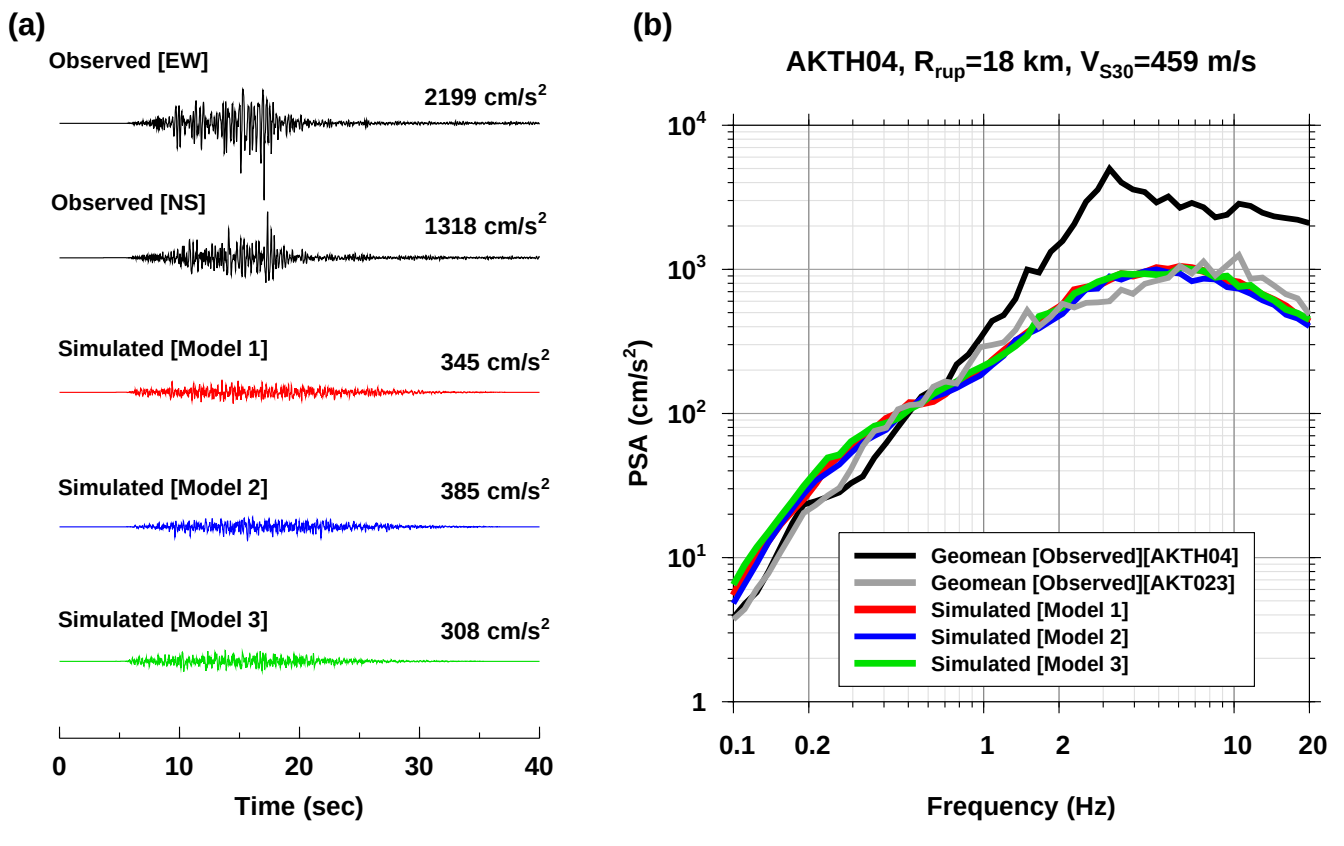
(a)
Observed [EW]
2199 cm/s2
Observed [NS]
1318 cm/s2
Simulated [Model 1]
345 cm/s2
Simulated [Model 2]
385 cm/s2
Simulated [Model 3]
308 cm/s2
0
10
20
30
40
Time (sec)
(b)
AKTH04, Rrup=18 km, VS30=459 m/s
PSA (cm/s2)
10^4
10^3
10^2
10^1
1
0.1
0.2
1
2
10
20
Frequency (Hz)
Geomean [Observed][AKTH04]
Geomean [Observed][AKT023]
Simulated [Model 1]
Simulated [Model 2]
Simulated [Model 3]

Figure_12.

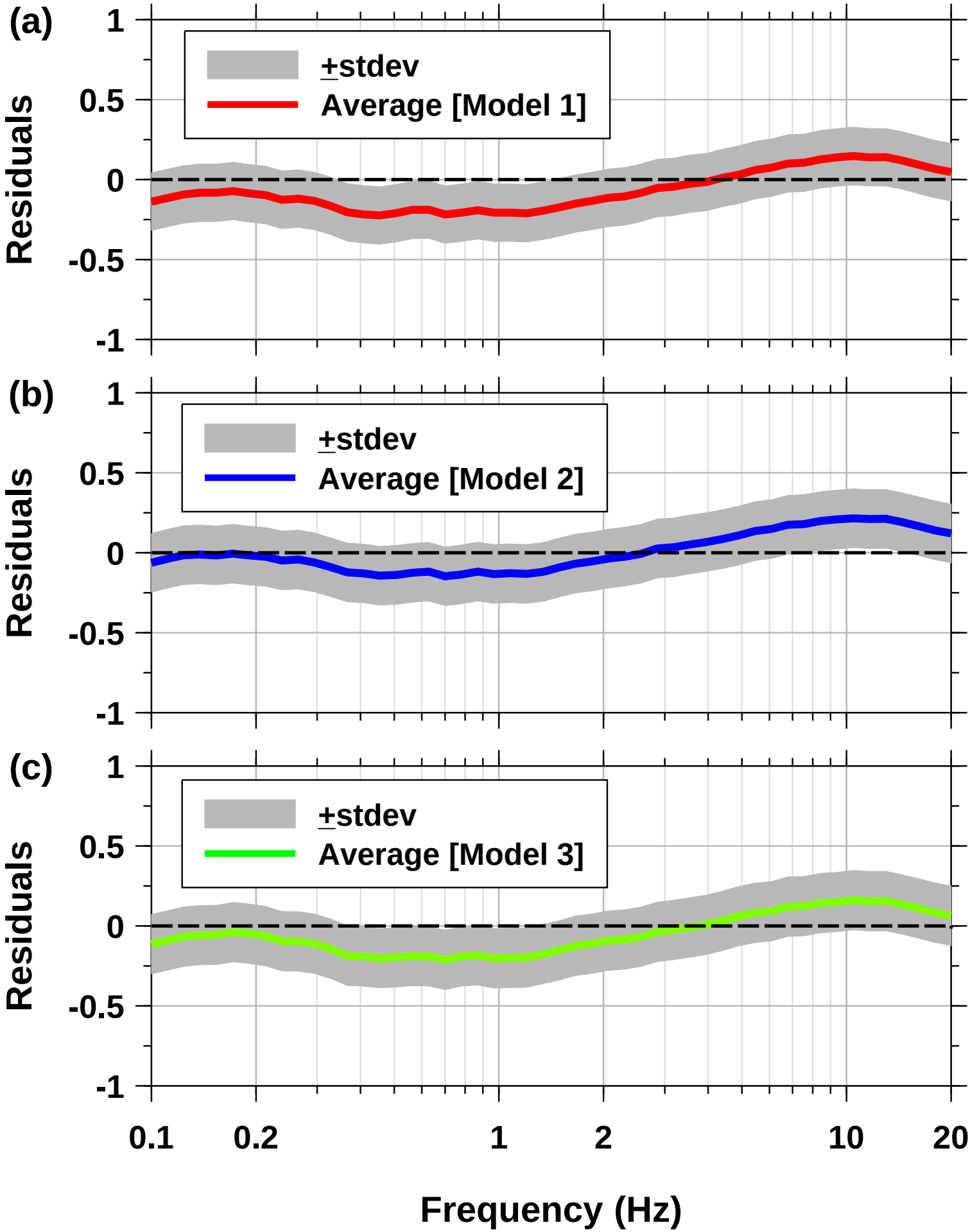
(a)
±stdev
Average [Model 1]
Residuals
1
0.5
0
-0.5
-1
(b)
±stdev
Average [Model 2]
Residuals
1
0.5
0
-0.5
-1
(c)
±stdev
Average [Model 3]
Residuals
1
0.5
0
-0.5
-1
0.1
0.2
1
2
10
20
Frequency (Hz)

Figure_13.

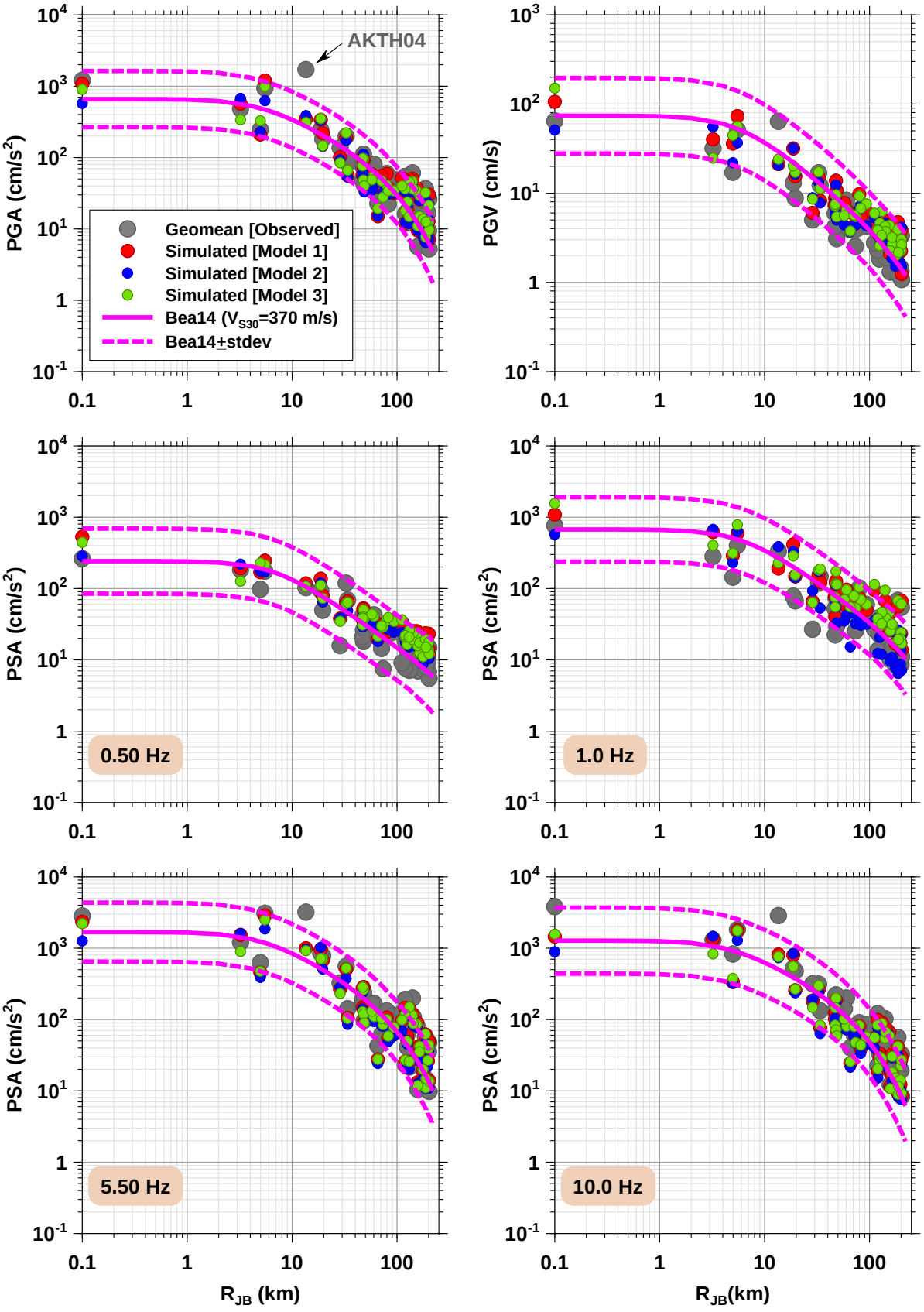
AKTH04
Geomean [Observed]
Simulated [Model 1]
Simulated [Model 2]
Simulated [Model 3]
Bea14 (V_{S30}=370 m/s)
Bea14±stdev
PGA (cm/s^2)
PGV (cm/s)
PSA (cm/s^2)
0.50 Hz
1.0 Hz
5.50 Hz
10.0 Hz
R_{JB} (km)
R_{JB}(km)